

Nature of Striation in 21 cm Channel Maps: Velocity Caustics

Yue Hu^{1,2*}, A. Lazarian^{2,3†}, D. Alina⁴, D. Pogosyan⁵, Ka Wai Ho²

¹*Department of Physics, University of Wisconsin-Madison, Madison, WI, 53706, USA*

²*Department of Astronomy, University of Wisconsin-Madison, Madison, WI, 53706, USA*

³*Centro de Investigación en Astronomía, Universidad Bernardo O'Higgins, Santiago, General Gana 1760, 8370993, Chile*

⁴*Department of Physics, School of Sciences and Humanities, Nazarbayev University, Astana 010000, Kazakhstan*

⁵*Department of Physics, University of Alberta, Edmonton, Alberta, T6G 2E1, Canada*

Accepted XXX. Received YYY; in original form ZZZ

ABSTRACT

The alignment of striated intensity structures in thin neutral hydrogen (HI) spectroscopic channels with Galactic magnetic fields has been observed. However, the origin and nature of these striations are still debatable. Some studies suggest that the striations result solely from real cold-density filaments without considering the role of turbulent velocity fields in shaping the channel's intensity distribution. To determine the relative contribution of density and velocity in forming the striations in channel maps, we analyze synthetic observations of channel maps obtained from realistic magnetized multi-phase HI simulations with thermal broadening included. We vary the thickness of the channel maps and apply the Velocity Decomposition Algorithm to separate the velocity and density contributions. In parallel, we analyze GALFA-HI observations and compare the results. Our analysis shows that the thin channels are dominated by velocity contribution, and velocity caustics mainly generate the HI striations. We show that velocity caustics can cause a correlation between unsharp-masked HI structures and far-infrared emission. We demonstrate that the linear HI fibers revealed by the Rolling Hough Transform (RHT) in thin velocity channels originate from velocity caustics. As the thickness of channel maps increases, the relative contribution of density fluctuations in channel maps increases and more RHT-detected fibers tend to be perpendicular to the magnetic field. Conversely, the alignment with the magnetic field is the most prominent in thin channels. We conclude that similar to the Velocity Channel Gradients (VChGs) approach, RHT traces magnetic fields through the analysis of velocity caustics in thin channel maps.

Key words: ISM:general—ISM:magnetohydrodynamics—turbulence—magnetic field

1 INTRODUCTION

Neutral hydrogen (HI) is the most abundant element in the universe, providing crucial information about galaxies' structure and evolution (Cox & Reynolds 1987; HI4PI Collaboration et al. 2016; Peek et al. 2018). In our Galaxy, studying the physical nature of HI intensity structures is essential to understanding the interstellar medium (ISM; Dickey & Lockman 1990), star formation processes (Mac Low & Klessen 2004; McKee & Ostriker 2007; Crutcher 2012), chemical evolution (Heckman et al. 1989; Wakker & van Woerden 1997; Hollenbach & Tielens 1999), and Galactic dynamics (Mihalas & Binney 1981; Kulkarni & Heiles 1988; Elmegreen & Scalo 2004).

The study of HI in astrophysics typically employs Position-Position-Velocity (PPV) cubes, where the sky coordinates of Position-Position are complemented with Doppler shift information in Velocity. The HI observation is commonly analyzed by slicing PPV cubes to create channel maps. Studies by Green (1993) and Stanimirovic et al. (1999) have shown that channel maps of the Milky Way and Small Magellanic Cloud respectively exhibit power-law statistics. The observed power spectrum and its variation with the

thickness of the channel maps were interpreted as a consequence of HI's non-linear spectroscopic mapping from Position-Position-Position (PPP) space to PPV space (Lazarian & Pogosyan 2000). In the process of this mapping, HI clouds with different line-of-sight (LOS) positions but similar LOS velocities can be sampled into the same location in PPV space. This causes the HI's intensity distribution in PPV space to appear crowded, morphologically distorted, and statistically modified. This phenomenon, called velocity crowding, is significant in ISM that is known to be turbulent (Armstrong et al. 1995; Chepurnov & Lazarian 2010; Xu & Zhang 2017; Ha et al. 2022; Yuen et al. 2022b).

Lazarian & Pogosyan (2000) developed the theory describing the velocity crowding effect and demonstrated that its significance is linked to the thickness of the channel map. In thin channels (i.e., with high-velocity resolution), the observed intensity structures of HI are significantly distorted. These intensity distributions are primarily created by velocity crowding, so their statistics are controlled by velocity rather than density statistics. The subsequent numerical studies (Esquivel et al. 2003; Chepurnov & Lazarian 2009; Padoan et al. 2009) confirmed the theoretical predictions. On the other side, it is well known that magnetohydrodynamic (MHD) turbulence is anisotropic, with turbulent eddies elongated along the magnetic fields (Goldreich & Sridhar 1995; Lazarian & Vishniac 1999; Federrath

* E-mail: yue.hu@wisc.edu

† E-mail: alazarian@facstaff.wisc.edu

2016; Tritsis et al. 2018; Beresnyak & Lazarian 2019; Beattie & Federrath 2020). This anisotropy is imprinted in the velocity crowding so that the intensity structures in thin channels are striated along the magnetic fields, denoted as HI striations. The theory of this effect was elaborated in Kandel et al. (2016) with anisotropies induced by three major MHD modes, solenoidal Alfvén mode, and compressive slow and fast modes, quantified (see also Yuen et al. 2023b).

The HI striations are critical for numerous studies, including tracing the Galactic magnetic field orientation at large scales (Yuen & Lazarian 2017; Lazarian & Yuen 2018a; Hu et al. 2020a; Lu et al. 2020), mapping the magnetic field strength of the diffuse ISM (Lazarian et al. 2018; Hu & Lazarian 2023a), and modeling the Galactic foreground polarization (Clark et al. 2015; Clark & Hensley 2019). For instance, Lazarian et al. (2002) proposed to use the anisotropy of HI striations measured in thin channel maps to trace magnetic field directions and study magnetization, introducing a new technique that was termed Velocity Channel Gradients (VChGs; Lazarian & Yuen 2018a). As an earlier separate development, Clark et al. (2014) used the linear-structure-detection algorithm, the Rolling Hough Transform (RHT), to identify the HI striations and reported an alignment with the Galactic magnetic field. However, the striations detected with RHT (denoted as RHT-fiber) were assumed to result from the actual Galactic HI cold density filaments (Clark et al. 2019).

The nature of striations in HI channel maps remains a hotly debated subject (Clark et al. 2019; Yuen et al. 2019; Peek & Clark 2019; Kalberla & Haud 2020; Yuen et al. 2021; Kalberla & Haud 2023). The controversy involves the applicability of the theory of Lazarian & Pogosyan (2000) to multiphase HI, where both cold and warm phases are present (McKee & Ostriker 1977). In particular, according to Clark et al. (2019), the alignment of RHT-fibers in thin channel maps results from the alignment of cold density filaments with magnetic field, while the effect of velocity caustics is negligible. The overlapping correlation of unsharp-masked (see § 7) GALFA-HI data (Peek et al. 2018) and far-infrared (FIR) Planck observations (Planck Collaboration et al. 2020) was employed to support this interpretation in Clark et al. (2019). However, the statistical significance of the correlation between HI and Planck was assessed using an unnormalized parameter. It was shown in Yuen et al. (2019) that after a proper normalization was introduced, this correlation is insignificant (see also Appendix A). In contrast, according to Lazarian & Yuen (2018a); Yuen et al. (2019); Hu et al. (2020b); Lu et al. (2020); Yuen et al. (2021), the striation revealed with the VChGS naturally arises from the anisotropy of velocity fluctuations in MHD turbulence.

In the present paper, we attempt to resolve the controversy above by exploring two approaches. The observational one separates channel maps' velocity and density contributions and evaluates their relative significance. This approach has already been explored in (Yuen et al. 2021) where the Velocity Decomposition Algorithm (VDA; Yuen et al. 2021) was introduced and successfully applied to GALFA-HI data. The other way is to analyze the synthetic observations obtained with multi-phase HI simulation and explore where the Lazarian & Pogosyan (2000) theory describing velocity crowding is applicable to describing channel maps. In what follows, we present a synergy of the approaches by analyzing thin channel maps obtained with synthetic observations of multi-phase HI, and applying the VDA both to these synthetic and actual GALFA-HI data. We explore the striation using the RHT and compare our findings with the results of earlier RHT studies. Throughout this study, we use the term "velocity caustics" to refer to HI striations that arise from turbulent velocity crowding. Notably, this term was previously used in the studies of cosmological Large Scale Structure to describe the enhancements

Run	M_S	M_A	Resolution	Condition	Code
Ms12MA06	1.2	0.6	792 ³	isothermal	ZEUS-MP/3D
Ms100MA07	10	0.7	792 ³	isothermal	ZEUS-MP/3D
MP	1.0	1.0	480 ³	multi-phase	Athena++

Table 1. Setups of numerical simulations. M_S and M_A are the mean values of the simulations.

of observed densities in the Hubble Flow as a function of redshift (Diemand et al. 2007; Vogelsberger et al. 2009).

The paper is organized as follows. In § 2, we describe this study's 3D numerical simulations and observational data. In § 3, we present numerical experiments to illustrate the velocity caustics and introduce the VDA pipeline adopted in this work. In § 4 and § 5, we present the results of our analysis, including numerical tests for VDA and the application of VDA to GALFA-HI data. In § 6, we show that comparing high-intensity HI structures within thin channels and FIR emission is inappropriate for testing the velocity caustics. In § 7, we discuss the nature of HI striations in thin channel maps and the implications of this work for other related studies. Our results are summarized in § 8.

2 NUMERICAL AND OBSERVATIONAL DATA

2.1 Numerical simulations

2.1.1 Isothermal simulations

This study uses 3D simulations of turbulence generated through the ZEUS-MP/3D code (Hayes et al. 2006). We briefly outline the setup for the simulations.

The ideal MHD equations, including mass density ρ and velocity \mathbf{v} , are solved with periodic boundary conditions. The equations are as follows:

$$\begin{aligned}
 \partial \rho / \partial t + \nabla \cdot (\rho \mathbf{v}) &= 0, \\
 \partial (\rho \mathbf{v}) / \partial t + \nabla \cdot \left[\rho \mathbf{v} \mathbf{v}^T + (c_s^2 \rho + \frac{B^2}{8\pi}) \mathbf{I} - \frac{\mathbf{B} \mathbf{B}^T}{4\pi} \right] &= \mathbf{f}, \\
 \partial \mathbf{B} / \partial t - \nabla \times (\mathbf{v} \times \mathbf{B}) &= 0, \\
 \nabla \cdot \mathbf{B} &= 0,
 \end{aligned} \tag{1}$$

where c_s is the constant sound speed due to the isothermal equation of state, and \mathbf{f} represents the stochastic forcing term used to drive turbulence. The magnetic field \mathbf{B} and density fields are initially set to be uniform, with \mathbf{B} aligned along the y -axis.

The turbulence simulations can be characterized by the sonic Mach number ($M_S = v_{\text{inj}}/c_s$) and the Alfvénic Mach number ($M_A = v_{\text{inj}}/v_A$) for MHD simulations, where $v_A = B/\sqrt{4\pi\rho}$ is the Alfvén speed. For turbulence driving, we adopt the common driving method (Cho & Lazarian 2003; Federrath 2013; Yuen & Lazarian 2017; Beattie & Federrath 2020). The energy injection is centered on wavenumber $k = 2\pi/l = 1 - 2$ (in the unit of $2\pi/L_{\text{box}}$, where L_{box} is the length of simulation box) in Fourier space, where l is the length scale in real space. We run the simulation for six eddy turnover times to ensure that the turbulence has reached statistical saturation. The values of M_S and M_A are listed in Tab. 1.

2.1.2 Multi-phase simulations

To emulate the multi-phase ISM environment, we incorporated an additional ordinary differential equation (ODE) solver to consider radiative cooling and heating effects in addition to the original Athena++ MHD Solver. Our initial state was a 3D turbulence box with periodic boundaries and a length of 200 pc, representing bulk neutral hydrogen in the ISM. We utilized a realistic synthetic cooling and heating function proposed by [Koyama & Inutsuka \(2002\)](#) and solved the equation with an adaptive implicit solver to ensure convergence. The simulation was initially of constant density and driven by spectral velocity perturbation in Fourier space. The multi-phase medium began to form approximately 20 Myr into the simulation. To ensure a realistic representation of a multi-phase medium and accurate capture of turbulence effects, we selected a snapshot around 100 Myr. The parameters for this snapshot are listed in Tab. 1. For additional simulation details and statistics, see [Yuen et al. \(2021\)](#) and [Ho et al. \(2021\)](#).

2.1.3 Synthetic spectroscopic observations

The observed intensity distribution of a given spectral line in PPV space is determined by both the density of emitters and their velocity distribution along the LOS. When coherent velocity shear, e.g. due to Galactic rotation (see Section 3.2) can be neglected, the LOS velocity component v is the sum of the turbulent velocity $v_{\text{tur}}(x, y, z)$, and the residual component due to thermal motions. This residual thermal velocity $v - v_{\text{tur}}(x, y, z)$, has a Maxwellian distribution $\phi(v, x, y, z)$, so that the gas distribution in PPV cubes, $\rho_s(x, y, v)$, and in real-space. This induces intensity fluctuation in PPV that for the case of emissivity proportional to density¹ provide PPV emission density $\rho_s(x, y, z)$ as ([Lazarian & Pogosyan 2004](#)):

$$\rho_s(x, y, v) = \kappa \int \rho(x, y, z) \phi(v, x, y, z) dz, \quad (2)$$

$$\phi(v, x, y, z) \equiv \frac{1}{\sqrt{2\pi c_s^2}} \exp\left[-\frac{[v - v_{\text{tur}}(x, y, z)]^2}{2c_s^2}\right], \quad (3)$$

where κ is a constant that relates the number of emitters to the observed intensities, which is not of interest to our discussion of the mechanism of caustic formation. $c_s = \sqrt{\gamma k_B T / m}$, with m being the mass of atoms or molecules, γ is the adiabatic index, k_B being the Boltzmann constant, and T the temperature, which can vary from point to point if the emitter is not isothermal. To include the thermal line broadening effect in the synthetic PPV cubes, $\rho_s(x, y, v)$ is convoluted by a thermal Gaussian kernel of $\sigma_T = c_s$.

By integrating $\rho_s(x, y, v)$ over a given velocity range, which is called the channel width Δv , we obtain a velocity channel:

$$p(x, y, v) = \int_{v-\Delta v/2}^{v+\Delta v/2} \rho_s(x, y, v') dv'. \quad (4)$$

If we split the 3D density into the mean density and zero mean fluctuations $\rho(x, y, z) = \bar{\rho} + \bar{\rho}\delta(x, y, z)$ we arrive at the representation of the channel intensity as the sum of two terms $p(x, y, v) =$

$$p_{vc}(x, y, v) + p_{dc}(x, y, v):$$

$$p_{vc} \equiv \int_{v-\Delta v/2}^{v+\Delta v/2} dv' \int \bar{\rho} \phi(v', x, y, z) dz, \quad (5)$$

$$p_{dc} \equiv \int_{v-\Delta v/2}^{v+\Delta v/2} dv' \int \bar{\rho} \delta(x, y, z) \phi(v', x, y, z) dz. \quad (6)$$

The first term contains the mean intensity in the channel and carries fluctuations that are produced exclusively by velocity mapping. To reflect this we can call this term pure "velocity" term as far as structures in intensity maps are concerned. The second, "density", term reflects inhomogeneities in the real 3D density, however, 3D density structures are still modified by velocity fluctuations when mapped to channel intensities.

In the case of $\Delta v = \infty$, we obtain the fully integrated intensity map I . The full line integrated p_{vc} is reduced to the mean column density while p_{dc} gives the column density variations on the POS. To generate a synthetic spectroscopic cube, we use the density field $\rho(x, y, z)$, velocity field $v_{\text{tur}}(x, y, z)$, and temperature information from simulations. Additionally, to produce p_{vc} , we use a constant density field $\rho(x, y, z)$ in PPP space so that pre-existing density structures are fully excluded.

2.2 Observational data: GALFA-HI and Planck

In this work, we utilize the GALFA-HI survey data from Data Release 2, as described in [Peek et al. \(2018\)](#). The HI data has a beam resolution of $4' \times 4'$, which has been gridded into $1' \times 1'$ per pixel, with a spectral resolution of ≈ 0.2 km/s and a brightness temperature noise of approximately 40 mK per 1 km s^{-1} integrated channel. Our analysis covers the full velocity range.

We use also the Planck 353 GHz data from the Planck 3rd Public Data Release (DR3) 2018 of High Frequency Instrument ([Planck Collaboration et al. 2020](#)). Observations from Planck designate the polarization angle ϕ with Stokes parameter maps I , Q , and U . Angle ϕ is defined as:

$$\phi = \frac{1}{2} \tan^{-1}(-U, Q), \quad (7)$$

where the $-U$ notation converts the angle from HEALPix convention to IAU convention. The Stokes parameter maps were smoothed from nominal angular resolution $5'$ to $16'$ with a Gaussian kernel to achieve a higher sign-to-noise ratio and match the resolution of the velocity channel gradients (see Appendix E). We infer the magnetic field angle from the equation: $\phi_B = \phi + \pi/2$.

3 ORIGIN OF THE STRIATION: DENSITY VERSUS VELOCITY EFFECTS

3.1 Toy model of velocity caustics

Fig. 1 illustrates the velocity crowding in PPV space due to spectroscopic mapping. Three constant-density clouds (n_1, n_2, n_3) are located at different spatial positions along the LOS in PPP space. n_1 and n_3 possess identical LOS velocities. As a result, these clouds are mapped into the same velocity coordinate in PPV space, leading to their merging into a single crowded cloud. This new cloud is not physically present in the PPP space but is rather created by the velocity crowding effect. n_2 with a larger LOS velocity is mapped into a different velocity coordinate.

In realistic scenarios, the mapping process is more complex due to the turbulent and magnetized nature of the ISM ([Armstrong et al.](#)

¹ The quadratic dependence of emissivity is considered in [Kandel et al. \(2016\)](#).

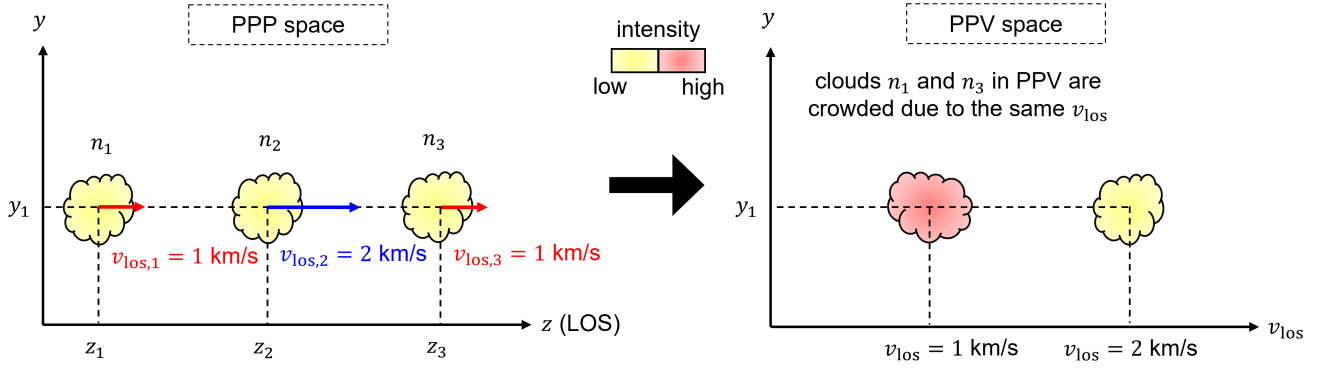


Figure 1. Illustration of velocity crowding. **Left:** three constant density (n_1, n_2, n_3) clouds in PPP space locate at different spatial positions along the LOS (z). n_1 and n_3 have identical LOS velocity v_{los} , while n_2 's LOS velocity is larger. **Right:** the three clouds are mapped into PPV space. Due to n_1 and n_3 's identical LOS velocities, they are crowded into only one cloud with higher density. The cloud's morphology gets different from those in PPP space and intensity increases.

1995; Chepurnov & Lazarian 2010; Crutcher 2012; Andersson et al. 2015). The turbulence leads to different parts of a cloud having distinct LOS velocities. Consequently, when mapped into PPV space, the cloud is substantially distorted, resulting in multiple HI clouds or sparsely distributed HI gas along the same LOS becoming crowded in PPV space. This crowding redistributes the HI gas in the PPV space and produces new HI intensity structures.

Fig. 2 presents a synthetic example of PPV cubes $\rho_s(x, y, v)$ generated from a density field $\rho(x, y, z)$ and the LOS component of the velocity field $v(x, y, z)$, accounting for thermal broadening effects. The density field $\rho(x, y, z)$ is a constant sphere, while the LOS velocity component v is derived from multiphase HI simulations. We can see the sphere in PPV space are considerably distorted. The constant $\rho(x, y, z)$ eliminates any pre-existing density structures that are correlated with the magnetic field so that the projected $\rho(x, y, z)$ map appears only as a circular structure (see Fig. 2, panel b). Moreover, we take spectral lines along three different LOS. The lines' amplitude is not constant, but varies as a function of velocity, resembling the line profiles obtained in observations. Then, in Fig. 2, panel (c), we take channel maps by using the spectral line averaged over the cube and vary the channel width (i.e., the velocity range used for integration). We can see a fully integrated channel recovers the column density map, erasing velocity information. The significance of crowding's significance is related to the channel width Δv . The velocity crowding effect gradually becomes more pronounced as the channel width decreases. In a thin channel map, the intensity structures become filamentary. These intensity structures are solely created by the velocity crowding effect.

3.2 Effect of the Galactic rotation

The LOS velocity in the ISM contains a contribution from Galactic rotation. It is commonly assumed that velocity information in spectroscopic PPV space can be used to determine the Galactic spatial location of observed objects using the Galactic rotation curve. However, the extent to which this is possible and over what distance scale it is possible is determined by comparing the LOS projected shear of Galactic rotational velocity with turbulent velocity over the same distance.

Lazarian & Pogosyan (2000) noted that in the vicinity of the Galactic plane, the coherent rotational shear is approximately 15 km/s

per kpc of separation (as given by Oort's constants) and is even smaller in high-latitude regions. The turbulent velocity, on the other hand, is typically around 10 km/s at 100 pc separation (Ha et al. 2022) and scales as the cubic root of separation l , i.e., $v_{\text{tur}} = v_{\text{inj}}(l/L_{\text{inj}})^{1/3}$. Therefore, at the injection scale $L_{\text{inj}} \sim 100$ pc to which turbulent cascade may extend, rotational velocity differences are only 1.5 km/s, which is one-sixth of turbulence injection velocity. Recovering LOS positions of HI parcels from the rotational curve within such distances in the presence of turbulent motions is very challenging. In this paper, we only briefly discuss the effect of Galactic rotation. One can refer to Lazarian & Pogosyan (2000) for details of the effect of rotational motion on velocity mapping.

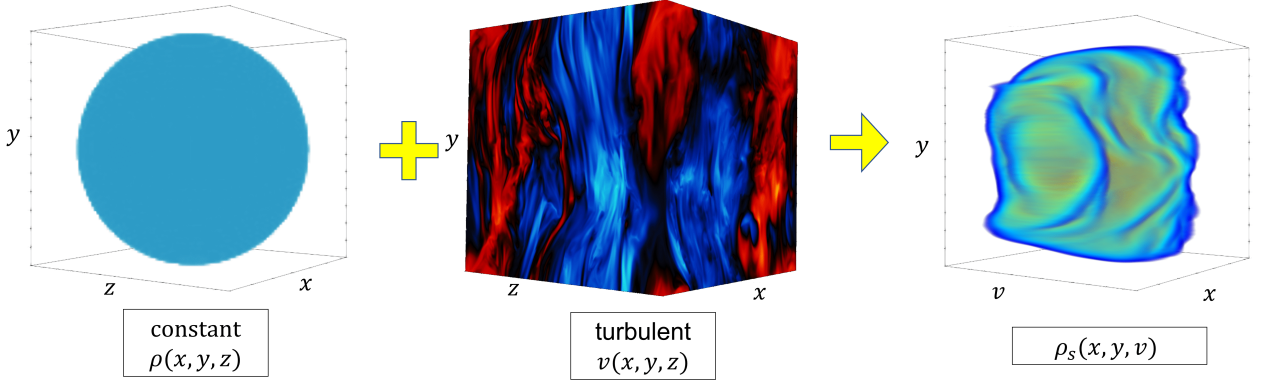
3.3 Effect of thermal broadening

Understanding the formation of velocity caustics in the presence of shear and thermal broadening can be achieved by considering the three settings below.

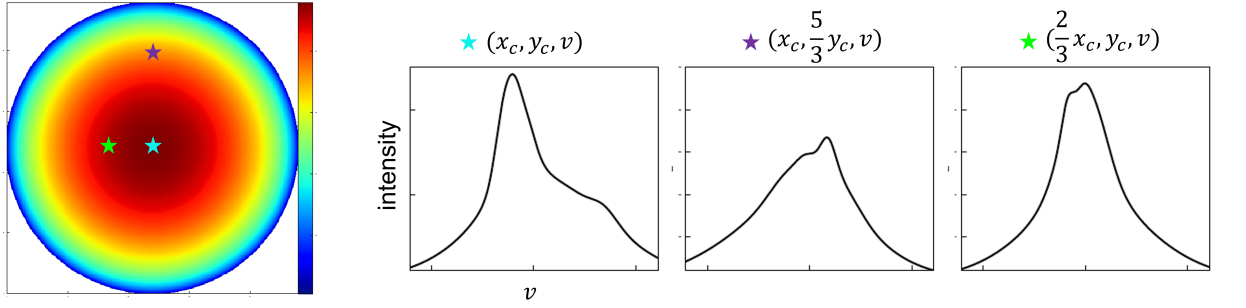
- **Setting 1.** Emitting atoms with zero thermal and turbulent velocities produce emission in one channel centered at $v = 0$. In this case, the channel thickness does not affect the observed intensities, and all the fluctuations arise from density fluctuations. If density filaments are present, their projected images are seen.
- **Setting 2.** Emitting atoms with thermal velocities and temperatures T produce emission in the range $\Delta v \sim \sqrt{k_B T/m}$, and all fluctuations arise from densities. When channels are thinner than $\sqrt{k_B T/m}$, the intensity of channel maps changes because only part of the total emission intensity of atoms (which is proportional to column density) is included in the range $\Delta v < \sqrt{k_B T/m}$. The change in channel width induces changes in intensity, so the intensity of fluctuations measured in a channel is correlated to the channel's thickness. However, with only thermal velocity considered, the morphological pattern of the intensity fluctuations in the velocity channel maps resembles that of the total integrated intensity, as well as column density (see Eq. 2). If a real density filament exists in this setting (i.e., with only thermal velocity), its projection on the POS can also be observed in the channel map.
- **Setting 3.** Emitting atoms have both thermal and turbulent velocities, leading to three sub-cases:

- (1). The regular velocity with shear only. In this case, the

(a) PPP → PPV



(b) Individual spectrum



(c) Averaged spectrum and channel map

Δv decreases, $\sigma_T = c_s$

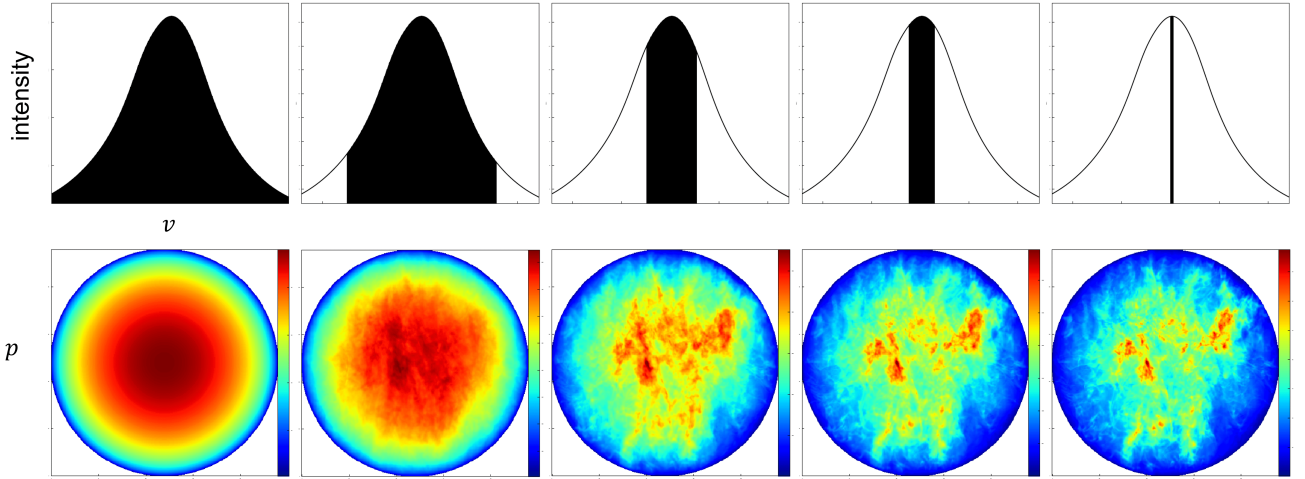


Figure 2. Panel (a): numerical 3D visualization of velocity caustics. The PPV cube $\rho_s(x, y, v)$ is generated with an input density field $\rho(x, y, z)$ and velocity field's LOS component $v(x, y, z)$ in PPP space. The density field $\rho(x, y, z)$ is a constant sphere, while the LOS velocity component v is adopted from the multiphase simulation. The mean magnetic field is oriented along the y -direction. **Panel (b):** spectral (three sub-plots on the right) of the synthetic PPV cube at three different positions on the $x - y$ plane. The three positions are labeled on the (left) integrated intensity map with star symbols. **Panel (c):** the velocity spectra (top) and channel maps p (bottom) of the PPV cube presented in panel (a). The velocity range used for integration (i.e., channel width Δv) is indicated by the shaded region in the top spectra (averaged over the full cube). Thermal broadening with a Gaussian kernel $\sigma_T = c_s$ is included.

velocity mapping provides a proxy for the third dimension, potentially providing insight into the emitter's distribution along the LOS. The intensity distribution observed in velocity channels can change².

– (2). Turbulent and thermal velocities only, no density fluctuations (i.e., emitting atoms uniformly distributed in PPP space). The turbulent velocities create intensity fluctuations, i.e., velocity caustics, in PPV space, as illustrated in Fig. 1. Due to thermal broadening, the intensity fluctuations raised from turbulent velocities in a channel might be erased or dominated by those raised by thermal velocities. Their relative significance depends on the temperature and channel width. For a given channel width, a higher temperature means a stronger thermal effect. However, when the channel width decreases, the significance of velocity caustics increases, so caustics are seen in thin channel maps (see Fig. B2).

– (3). Both velocity and density contributions affect the intensity distribution in channel maps, but their relative importance, p_v and p_d , varies with the thickness of the channel map. When a thick channel is integrated over a large velocity range, such as the entire velocity range, only a column density map with no velocity information is obtained (see Fig. 2). However, as the channel width decreases, the contributions from densities decrease while the velocity contributions increase. When the channel width is less than the turbulence velocity dispersion, σ_v , the velocity contribution dominates over the density contribution, provided that the mean density is greater than the density fluctuation (see Lazarian & Pogosyan 2000 for a more detailed discussion). Note that in any case, the p_d term in the thin channel regime is not a pure spatial density perturbation but is also modified by velocity mapping.

Settings 1 and 2 are straightforward, while Setting 3 (1) is widely discussed in the literature as a means of mapping the 3D distribution of emitters using the Galactic rotation curve. However, a caveat of this setting is the absence of turbulent velocities. In the presence of turbulence, a narrow velocity channel may not accurately represent the actual density distribution along the LOS. Nevertheless, the turbulence effect can be mitigated by increasing the thickness of the channel maps. Furthermore, as indicated in Setting 3 (2) and (3), we know that (i) the thermal effect can decrease the velocity contribution in a channel, and (ii) the relative significance of velocity caustics depend on the thickness of the channel maps. In Figs. B1 and B2, we showed the thermal effect at a normal level and density contribution are sub-dominated in thin channels using isothermal MHD simulations. Nevertheless, in the following, we introduce how to separate the thermal effect and p_d from a channel.

3.4 Separating velocity contribution and removing thermal broadening

To understand the origin of the elongated HI structure within thin channels, it is crucial to identify a suitable and dependable way to separate the velocity and density contribution, as well as remove thermal broadening, in PPV channels. Then one can directly test the velocity caustics effect. Theoretical separation is given by Eqs. (5, 6) that generates a pure velocity caustics contribution, p_{vc} can be accomplished in simulations by using a constant density field $\rho(x, y, z)$ in PPP space and simulated velocity $v(x, y, z)$. It is, however, difficult to apply directly to observational channel data, since the mean

² As we discussed in § 3.2, the turbulent velocity shear increases with the decrease of the scale, the effects of shear arising from Galactic rotation has little effect on velocity caustics at small scales.

spatial density is unknown. To overcome this difficulty, Yuen et al. (2021) introduced a novel technique named Velocity Decomposition Algorithm (VDA).³ In this paper, we discuss the VDA only briefly, with additional details to be found in Yuen et al. (2021).

From the intensity distribution within a channel, denoted as $p(x, y, v)$, VDA extracts the velocity $p_v(x, y, v)$ and density $p_d(x, y, v)$ contributions in the channel according to the following prescription:

$$p_d = (\langle p \cdot I \rangle - \langle p \rangle \langle I \rangle) \frac{I - \langle I \rangle}{\sigma_I^2},$$

$$p_v = p - p_d = p - (\langle p \cdot I \rangle - \langle p \rangle \langle I \rangle) \frac{I - \langle I \rangle}{\sigma_I^2},$$
(8)

where $I \equiv \int_{-\infty}^{\infty} dv p(x, y, v)$, $\sigma_I^2 = \langle (I - \langle I \rangle)^2 \rangle$ and $\langle \dots \rangle$ denotes the ensemble average over the entire map⁴. Defined this way, p_d describes the channel intensity fluctuations proportional to column density fluctuations at the level given by the cross-correlation coefficient between channel and column intensities. The "velocity" part p_v contains the contribution from the pure velocity part p_{vc} .

In addition, it is worth noting that p_v and p_d have the following fundamental properties:

$$\langle p_d \rangle = 0, \quad \int_{-\infty}^{\infty} dv p_d(x, y, v) = I - \langle I \rangle,$$

$$\langle p_v \rangle = \langle p \rangle, \quad \int_{-\infty}^{\infty} dv p_v(x, y, v) = \langle I \rangle,$$

$$\langle p_v p_d \rangle = 0,$$
(10)

which highlights firstly the fact that p_d is a perturbative term, carrying information only about density inhomogeneities, while p_v contains the mean intensity background and velocity field contribution, and secondly the orthogonality of VDA decomposition in the sense that p_d and p_v are uncorrelated.

The values p_v are available directly via the application of VDA to observations. On the contrary, the quantity p_{vc} is only available using numerical simulations with a constant density and serves as a theoretical template for the structures generated purely by velocity mapping. The value of the chosen constant density rescales p_{vc} . Thus, if the density is significantly non-uniform, the magnitude of p_{vc} will depend on which volume the mean density is determined. For instance, if one studies the small scale structure of a cloud, the appropriate value of the mean density entering velocity mapping is that of a cloud, rather than the lower value averaged over wider emptier space. This rescaling of p_{vc} , however, does not change the shape of the structures that this part of the signal exhibits.

Respectively, it is important to acknowledge the limitations inherent in the VDA approach. The VDA model assumes the presence of

³ The effectiveness of the VDA has been thoroughly tested using multi-phase HI simulations and GALFA-HI data (Yuen et al. 2021, 2023a). While the validity of the VDA was strongly questioned by Kalberla et al. (2022), this paper was based on the error in the understanding of the VDA. This was pointed out in Yuen et al. (2022a), and the aforementioned authors retracted their paper from A&A.

⁴ In observation, p and I can be obtained from:

$$p(x, y, v) = \int_{v-\Delta v/2}^{v+\Delta v/2} T_{mb}(x, y, v') dv',$$

$$I(x, y) = \int_{-\infty}^{+\infty} T_{mb}(x, y, v') dv',$$
(9)

where T_{mb} is the brightness temperature.

a single emitting turbulent region with velocity and density fluctuations. While this assumption is accurate for a turbulent cloud, such as a localized molecular cloud, it becomes problematic when dealing with HI gas that consists of multiple components along the LOS. In such cases, the application of VDA would result in the cumulative density of all the components being represented by p_d . To mitigate this issue, the VDA can be applied to the emission line decomposed into Gaussian components, as described in [Hu et al. \(2022b\)](#). Furthermore, the accuracy of determining $\langle I \rangle$ can be affected by an inhomogeneous intensity distribution across the analyzed image. To address this, it is possible to filter out low spatial frequencies of the image or apply the VDA to sub-blocks of data. These improvements are particularly relevant when applying the VDA to HI in the Galactic disk that exhibits multiple peaks. In the present study, we include three clouds in both high and low galactic latitudes. This allows us to emphasize the importance of considering velocity caustics in our analysis.

Bearing this in mind, we proceed to analyze a multi-phase simulation of magnetized HI, which will enable us to determine whether the striation observed in channel maps arises from velocities or densities.

4 NUMERICAL TESTING: MULTI-PHASE HI SIMULATIONS

4.1 Multiphase HI simulations

4.1.1 Tests for VDA

In this section, we apply VDA to synthetic observation with the purpose of determining the relative level of "density" p_d and p_v contributions as well as analyzing the level at which p_v can be explained by the pure velocity caustic effect as encoded in p_{vc} . In simulations, p_{vc} is the result of using simulation velocities and applying them to constant density (as in Fig. 2). At the same time, p_v is the result of VDA separation of the effect of velocity caustics from the effect of density fluctuation. A numerical test of VDA's validity in removing thermal broadening and separating velocity contributions using isothermal MHD simulations is given in Fig. B2. In the main text, we directly start with the multi-phase simulation. More on the VDA justification and application can be found in [Yuen et al. \(2021\)](#).

In Fig. 3, we perform VDA in $M_S = 1.0$, $M_A = 1.0$ multi-phase HI MHD simulation and compare obtained p_v and p_d with the pure velocity contribution p_{vc} and the full channel intensity p . Different from isothermal MHD simulations, the multi-phase simulation is not scale-free and is composed of the cold neutral medium (CNM), unstable neutral medium (UNM), and warm neutral medium (WNM). The comparison is performed for three channels centering at different v_{los} . The channel associated with the most prominent intensity is denoted as the central channel and the other is called the wing channel.

We can see that for both the central and wing channels, intensity structures in p are similar to those in velocity contribution p_v and velocity caustics p_{vc} . This means velocity caustics has an important contribution to channel maps. The perturbative quantity p_d is allowed to have negative values and its amplitude varies because p_d contains the information of density fluctuations in a channel. Nevertheless, the difference between central and wing channels exists. For the central channel, the similarity also appears between p and p_d , while this is not observed in the wing channel. It suggests p_d has more contribution to the central channel, while p_v is still dominated. In both cases, the correspondence of p_v and the velocity caustics p_{vc}

tests the performance of VDA with synthetic observations of multi-phase HI. In short summary, Fig. 3 testifies that:

- The contributions to channel p arising from density p_d and velocity p_v are different.
- Structures observed in thin velocity channels p are dominated by velocity contribution p_v . The effect of density variations p_d is marginal for thin velocity channels, especially the wing channel.
- The correspondence of the p_v and p_{vc} is very good (quantification is given in § 5.1). Thus, p_v obtained via VDA can be used as a proxy for p_{vc} where the information on the mean density is unavailable and VDA provides a tool for separating density and velocity contributions to intensity striations observed in the PPV channel, irrespective of the thermal effect's significance (see Fig. B2).

We discuss the application of VDA to actual HI observational data in § 5.

4.1.2 Nature of striations in thin channels

The 3D visualization of the multi-phase HI simulation's density cube in PPV space is given in Fig. 4 (left side). It shows many high-density filaments can be aligned either parallel or perpendicular to the magnetic field that is shown by black lines. The comparison between the upper and lower left panels shows that the dense structures correspond to cold gas. The highlighted magenta squares show that the magnetic field is mostly vertical, and the cold density structures/filaments are preferentially horizontal. This confirms that PPP cold-density filaments are not necessarily parallel to magnetic fields which corresponds well to theoretical expectations ([Xu et al. 2019](#)). Similarly, these (perpendicular) cold density filaments are also observed in [Gong et al. \(2023\)](#) using multi-phase simulations (see their Fig. 10).

To objectively analyze the velocity caustics' impact on shaping the intensity distribution in PPV space, we plot six thin channel maps ($\Delta v \approx 1.5$ km/s) generated from the multi-phase simulation and located at different velocity coordinates, covering almost the entire velocity range. In all these channel maps, we observe the intensity structures preferentially follow the magnetic field. This is also true for the regions where the cold-density structures tend to be perpendicular to the magnetic field. This testifies that the density contributions are subdominant to what is seen in the channel maps.

To better visualize the striated intensity structures in thin channel maps, we follow [Clark et al. \(2015\)](#) and employ the Rolling Hough Transform (RHT; [Clark et al. 2014, 2015](#)), which is an algorithm for extracting linear structures in an image. The RHT results depend on the somewhat arbitrary input parameters ([Clark et al. 2014](#)) of smoothing kernel diameters (DK), a window diameter (DW), and an intensity threshold (Z). Different parameters may affect the degree of alignment of "fibers" with the magnetic field (see Figs. 5, 6, 7 in [Clark et al. 2014](#)). We repeated the RHT analyses with different parameters and selected the "visually correct" result with parameters of $DK = 11$, $DW = 55$, and $Z = 0.7$. For this choice of parameters, the RHT provides a better tracing of the magnetic fields.

In Fig. 4 (right side), we present the RHT-identified structures (i.e., RHT-fibers) for the six channel maps. Looking at the magenta squares it is easy to see that the cold-density filaments perpendicular to the magnetic fields seen in PPP space are not seen in thin channel maps. The RHT-identified filaments are aligned parallel to the projected magnetic field. Using the synthetic p_{vc} maps obtained with constant density, we observe that RHT-fibers obtained for p_{vc} are nearly identical to the fibers thin channel maps p . This proves that RHT-fibers in thin channel maps arise from velocity caustics.

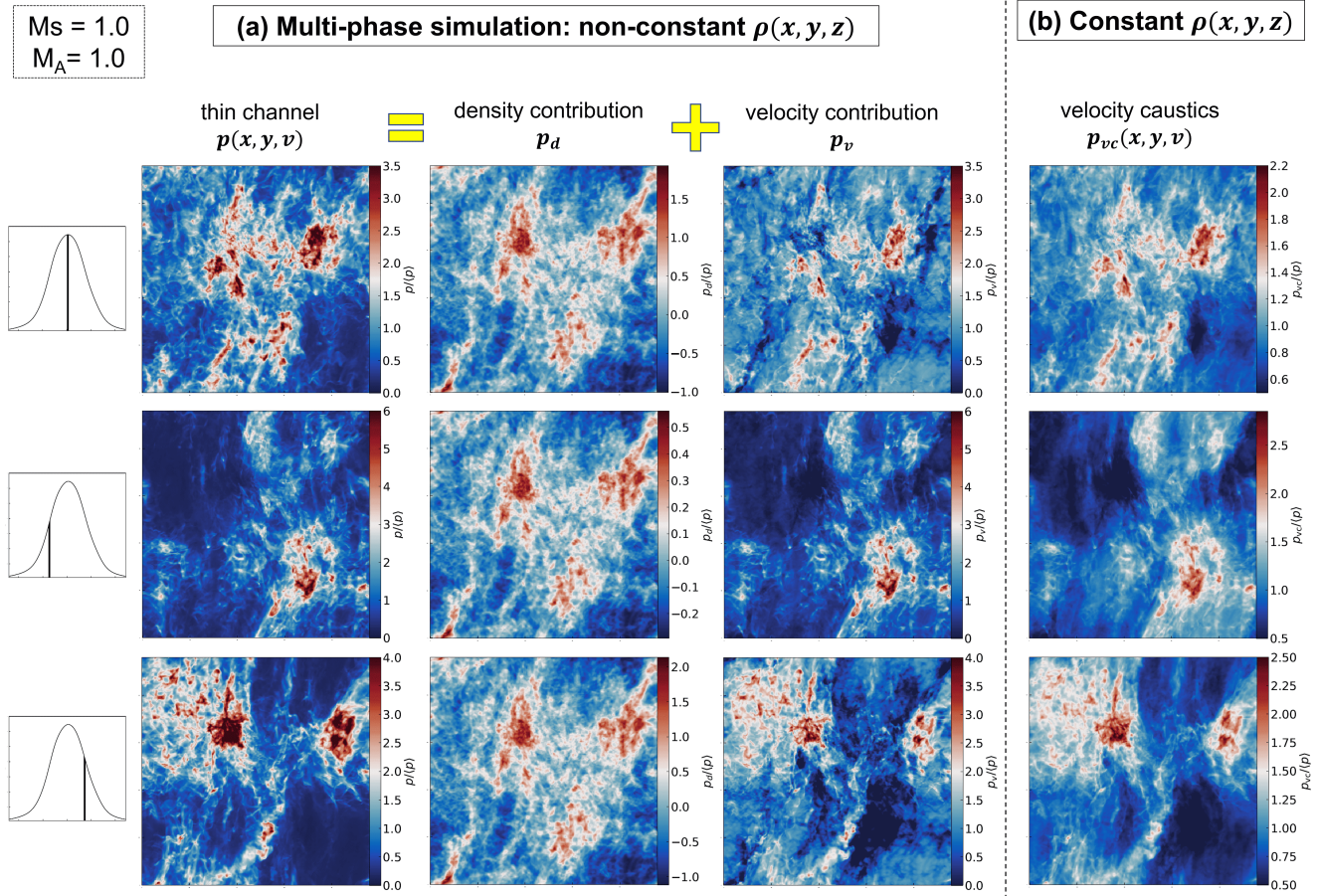


Figure 3. Schematic of the formation of images velocity channel maps and their comparison with velocity caustics. **Panel (a):** Results of the separation of density contribution (p_d) and velocity contribution (p_v) from a thin channel (p) using a non-constant 3D density field ρ from the MHD simulations. The velocity range used for integration is indicated by the shaded region in the top spectrum. The color bars for panels provide the relative contributions. The left graphs show the position of the channels relative to the average profile of the line **Panel (b):** The thin channel p_{vc} in this panel was generated using a constant density field equal to the full volume mean density, thereby eliminating any pre-existing density structures. The structures within the thin channel are solely created by velocity mapping. The integration velocity range is identical to that in panel (a). The mean magnetic field is oriented along the vertical y -direction and thermal broadening is included. The channel width ≈ 0.2 km/s is selected to match the GALFA-HI data.

The alignment of RHT-fibers with magnetic field in our synthetic observations is similar to that was observed earlier in GALFA-HI data (see [Clark et al. 2014, 2015](#)). This suggests that striations of intensity observed in GALFA thin channel maps are dominated by velocity caustics rather than cold-density PPP filaments. Further in the paper (see §5.2), we strengthen this conclusion by applying VDA to GALFA data.

Note that our analysis does not mean that cold HI filament cannot be aligned with the magnetic field, but shows that the contribution of these filaments is subdominant for RHT-filaments detected in thin channel maps. Indeed, if we examine PPP filaments beyond the magenta square, we observe cold filaments parallel aligned with magnetic fields, as seen in Fig. 4. Such alignment is expected in MHD turbulence theory ([Xu et al. 2019; Beattie et al. 2021](#)) e.g., if turbulent velocities passively advect the density fluctuations. This is, for instance, the case for density inhomogeneities arising from entropy fluctuations when turbulent gas is not isothermal. In this case, the statistics of density fluctuations mimic the statistics of the velocity ([Monin & Yaglom 2013](#)), and therefore the parallel alignment of density filaments is expected in PPP space. Thus, the velocity field

is responsible for the parallel (to magnetic field) alignment of both RHT-fibers in thin channel maps and the occasional alignment of cold-density filaments.⁵

In other words, the correspondence of the alignment of filaments observed in high Galactic latitude FIR maps and the RHT-detected fibers in channel maps (see Fig. 1 in [Peek & Clark 2019](#), Fig. 8 in [Clark et al. 2019](#), and Fig. 9 in [Kalberla & Haud 2020](#)) cannot be used as an argument that the RHT fibers are images of PPP cold density filaments. In § 7, we present another example: FIR filaments are perpendicular to magnetic fields.

In summary, our analysis of synthetic observations obtained with multi-phase HI reveals:

- Some PPP cold-density filaments in multi-phase HI are perpendicular, while others are parallel to the ambient magnetic field.
- These cold-density filaments marginally affect the striations observed in thin velocity channel maps.

⁵ When the back reaction from the gas is important, the parallel to magnetic field alignment is not enforced, in agreement with our simulations.

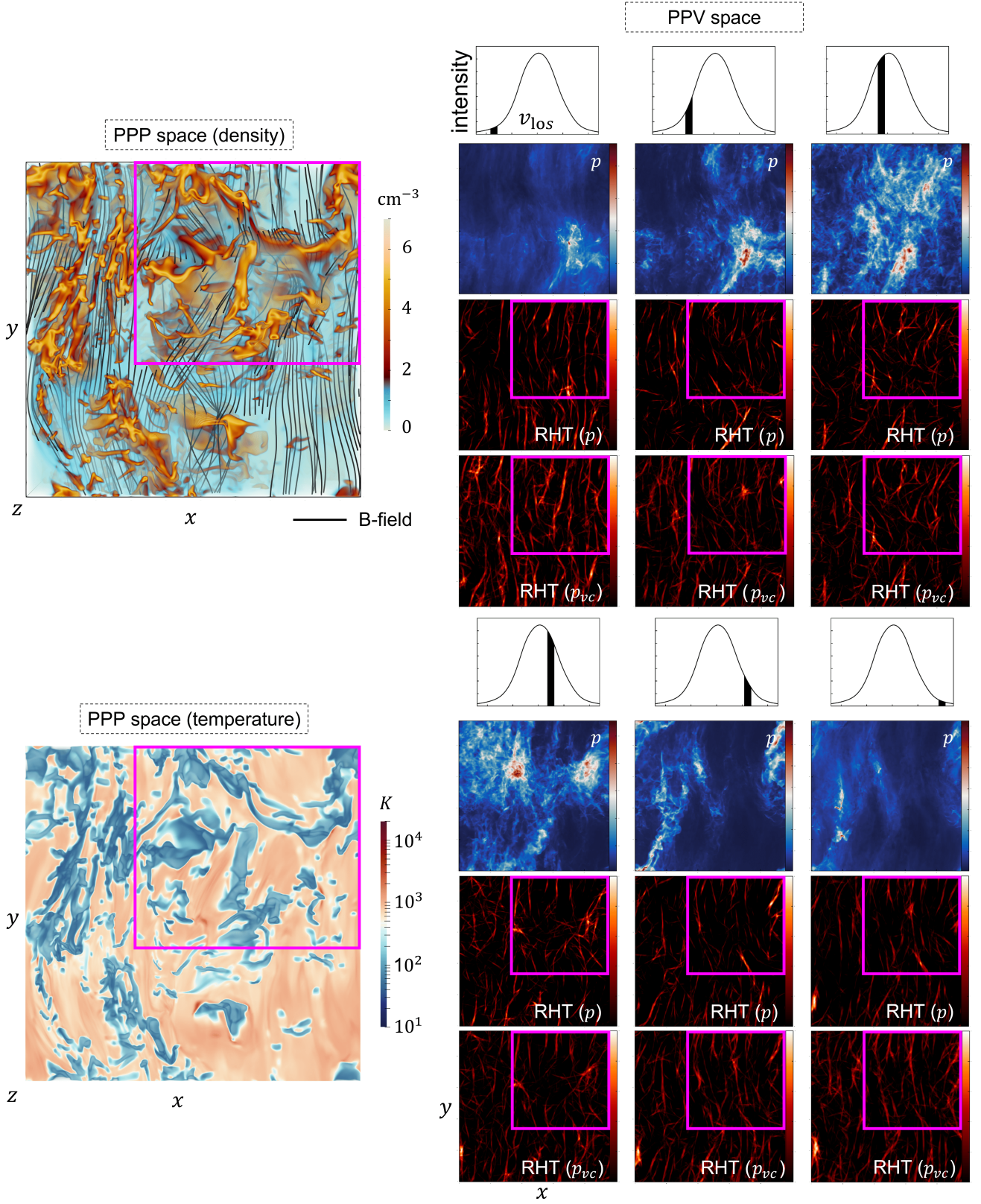


Figure 4. **Left:** 3D visualization of the multi-phase simulation's volume density field and magnetic field (top), as well as temperature (bottom), in PPP space. In the highlighted square box specifically, one observes density structures that are mostly orthogonal to the magnetic field. **Right:** synthetic thin ($\Delta v \approx 1.5$ km/s) channel maps p generated from the multi-phase simulation and their corresponding RHT-fibers. The RHT-maps are calculated from p and their corresponding p_{vc} maps, which are generated from a constant density field. Thermal broadening is included. The shaded area at the top spectra indicates the velocity range used for integration.

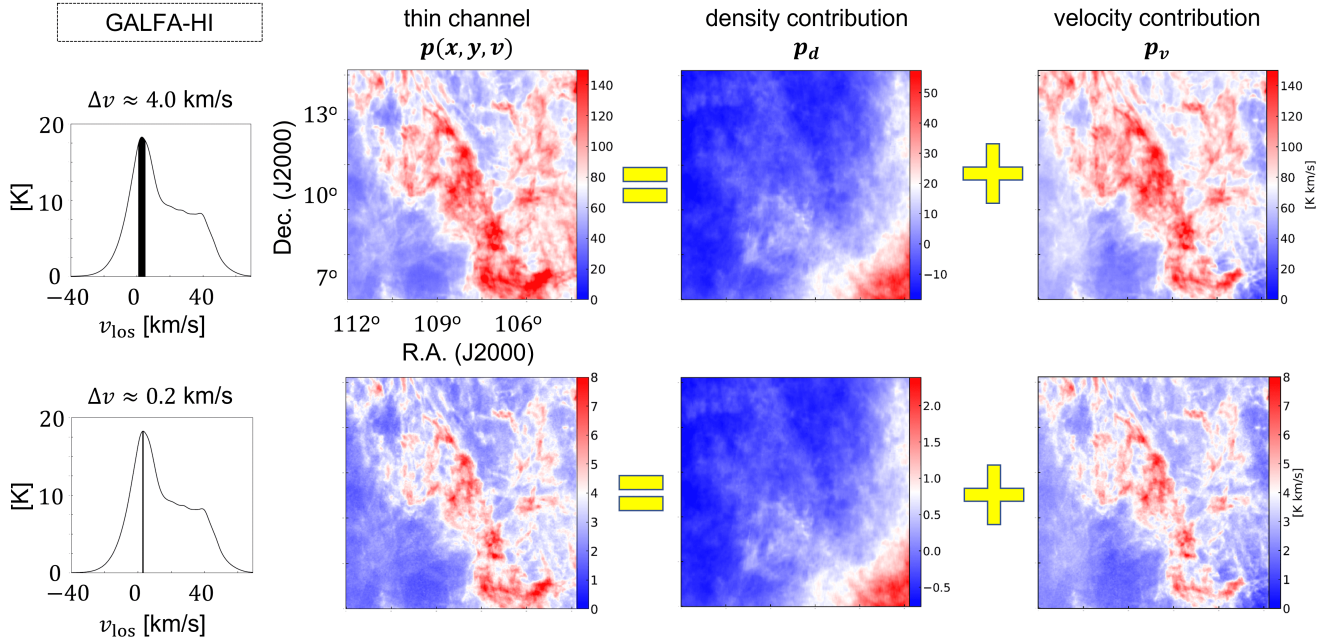


Figure 5. Same to Fig. 3, but for a HI cloud ($v_{\text{los}} \approx 3$ km/s) selected from the GALFA-HI survey. The shaded area at the top indicates the velocity range (i.e., channel width Δv) used for integration. Two different channel widths have been adopted: $\Delta v \approx 4.0$ km/s (top) and $\Delta v \approx 0.2$ km/s (bottom).

- RHT applied to thin channel maps delivers striations that arise from velocity caustics, and these RHT-fibers are parallel to the magnetic field.

5 VDA'S APPLICATION TO HI OBSERVATIONAL DATA

5.1 Dominance of velocity caustics in thin channels

In § 4, we presented a simulation-based visual comparison between the VDA-separated velocity contribution p_v in a thin channel and the pure velocity caustics channel. In this section, we provide an observational example using GALFA-HI data and quantify the significance of velocity caustics.

Fig. 5 displays two channel maps of the HI cloud, located at $v_{\text{los}} \approx 3$ km/s but with different channel widths ($\Delta v \approx 4.0$ km/s and $\Delta v \approx 0.2$ km/s). Noticeable differences can be observed between p_d and p_v . In addition, p_d associated with low intensity has only a marginal contribution to the high-intensity filamentary striations observed in p . On the other hand, structures seen in p are highly similar to those in p_v , in terms of topology and intensity amplitude. This suggests that both channels ($\Delta v \approx 4.0$ km/s and $\Delta v \approx 0.2$ km/s) are dominated by prominent velocity caustics. Two more examples at different Galactic latitudes are given in Fig. D1.

5.1.1 NCC analysis

We further use the normalized covariance coefficient (NCC) to quantify the correlation between p_v and other maps. NCC of two maps A and B is defined as (Yuen et al. 2019):

$$\text{NCC} = \frac{\langle (A - \langle A \rangle)(B - \langle B \rangle) \rangle}{\sigma_A \sigma_B}, \quad (11)$$

where σ_A and σ_B represent the standard deviation of maps A and B , respectively. NCC ranges from -1 to 1, with $\text{NCC} = 1$ indicating

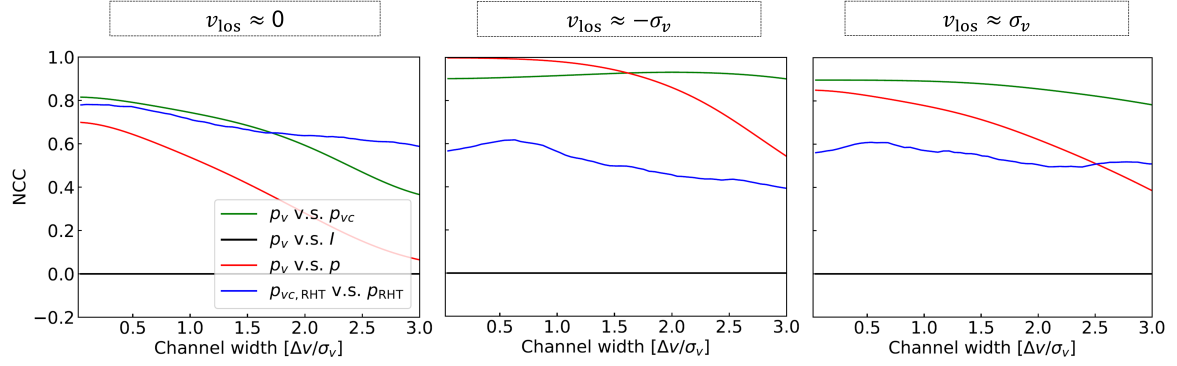
that the two maps A and B are statistically perfectly correlated. $\text{NCC} = 0$ and $\text{NCC} = -1$ correspond to the two maps being statistically uncorrelated and anticorrelated, respectively. NCC focuses on the comparison of the structures' morphology in two maps, rather than on their relative magnitudes, to which the NCC coefficient is insensitive.

Fig. 6 displays the correlation between normalized NCC and channel width for the multi-phase simulation, as well as the GALFA-HI cloud. We start with the case of the simulated central channel associated with the most prominent intensity. The numerical comparison reveals a strong correlation between p_v and p_{vc} , with $\text{NCC} \sim 0.8$ when the channel is *thin*, $\Delta v / \sigma_v < 1$ (Lazarian & Pogosyan 2000). Given that p_{vc} is generated from a constant density field and contains solely velocity information, this high NCC value implies that p_v reveals velocity structures. Concurrently, a strong correlation ($\text{NCC} \sim 0.7$) is detected between p_v and p , contrasting with the absence of any correlation with the column density I . The correlation between p_v and p diminishes as the channel width increases, an expected outcome since a thicker channel integrates more density contributions.

To better understand the origin of RHT-fibers, we employ RHT to process p_{vc} and p maps using the same parameters as those in Fig. 4, resulting in $p_{vc, \text{RHT}}$ and p_{RHT} respectively. As shown in Fig. 6, $p_{vc, \text{RHT}}$ and p_{RHT} always display a strong correlation with $\text{NCC} > 0.6$ regardless of the channel width. Considering $p_{vc, \text{RHT}}$ contains only velocity information, this confirms that the shapes of the observed RHT-fibers in p_{RHT} to a large extent follow velocity caustics.

In addition to the central channel, we repeat the NCC analysis for two more channels centering at $v_{\text{los}} \approx \pm \sigma_v$, called wing channels. We found that NCC values of p_v v.s. p_{vc} and p_v v.s. p in the wing channels are higher than in the central channel, even achieving $\text{NCC} > 0.9$ when $\Delta v / \sigma_v < 1$. This would suggest that the velocity contribution is more significant in wing channels. This effect, however, is in part due to large scale motions which separate high velocity regions into

(a) Multi-phase simulation



(b) GALFA-HI

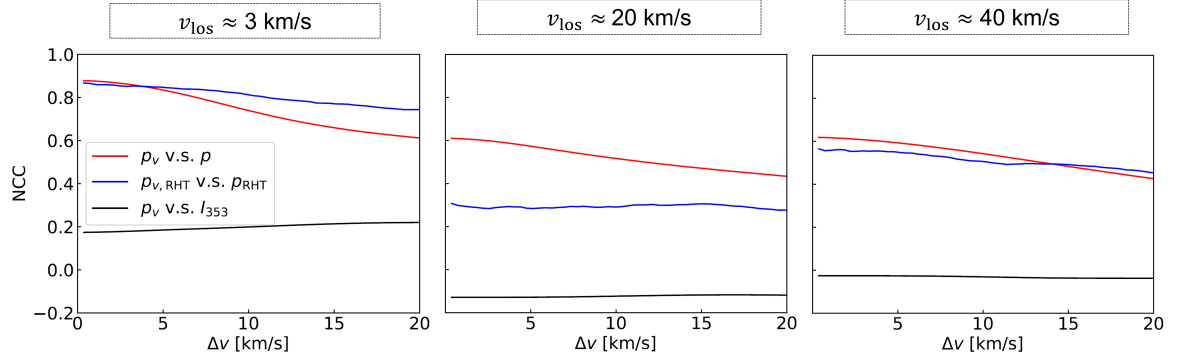


Figure 6. Panel (a): This panel displays the dependence of NCC on channel width Δv , normalized by the velocity dispersion σ_v . NCC values range from -1 to 1, where 1 represents a perfect correlation, 0 indicates no correlation, and -1 represents anti-correlation. NCC is calculated between the velocity contribution p_v , thin channel maps p , column density map I , and pure velocity caustics map p_{vc} . The column density map I is integrated along the full LOS velocity range to erase velocity information. p_{RHT} and $p_{vc,\text{RHT}}$ are the RHT-processed p and p_{vc} maps, respectively. Panel (b): This panel presents the NCC values between the p_v , p , and Planck 353 GHz FIR intensity map I_{353} for the GALFA-HI cloud (see Fig. 5). The Planck map only contains density information in the cold phase. v_{los} refers to the central LOS velocity of the channels. $p_{v,\text{RHT}}$ is the RHT-processed p_v map.

different channels. When we filter out the large scale modes in RHT analysis, we find the correlation between $p_{vc,\text{RHT}}$ and p_{RHT} in wing channels, while still rather strong, $\text{NCC} \sim 0.6$, to be somewhat lower than in the central channel.

Next, we calculated the NCC for the GALFA-HI cloud at three different $v_{\text{los}} \approx 3, 20$, and 40 km/s. Here, with p_{vc} not available, we limit ourselves with comparing p_v to the raw channel p and the Planck 353 GHz FIR map I_{353} . As Fig. 6 shows, p_v is highly correlated with p when the channel is narrow. In particular, NCC exceeds 0.6 when $\Delta v \approx 0.2$ km/s. In the central channel, NCC values are as high or higher as in the simulations, however in the wings they are lower. The processed $p_{v,\text{RHT}}$ maps also show a high correlation with the p_{RHT} in the central channel, at the same level of $\text{NCC} \sim 0.8$ as $p_{vc,\text{RHT}}$ showed in the simulations. This provides observational evidence that RHT-fibers here originate from velocity caustics. However in the wings $p_{v,\text{RHT}}$ behaviour is less consistent than that of a simulated $p_{vc,\text{RHT}}$. We expect that the existence of multiple HI clouds together with shear velocity makes it challenging to interpret wing channels, which in simulations are defined for a single HI cloud. In addition, we have replicated our analysis for two more clouds, including a high-latitude one (see Appendix D). These clouds exhibit still high NCC values for p_v versus p , hinting at the prevalence of velocity caustics.

Additionally, the NCC values between p_v and I_{353} range from -0.2 to 0.2, suggesting an insignificant correlation. The value is not strictly zero since I_{353} is not the column density exactly. A similar

comparison of p and the Planck FIR map was conducted in Clark et al. (2019). However, they used an unnormalized parameter to quantify the correlation. This correlation was proven to be insignificant in later studies (see Appendix A and Yuen et al. 2019).

5.2 RHT fibers in thin channels originate from velocity caustics

In § 4.1, we used the synthetic channel maps obtained with simulations of magnetized multi-phase HI to demonstrate that the RHT-fibers in the thin velocity channel maps arise from velocity caustics. Below we gauge the relative effect of velocity and density contributions to RHT-fibers in GALFA channel maps. This study is important as the striations of HI structures within thin channels processed with RHT were proposed to trace the magnetic fields (Clark et al. 2014, 2015). That study, however, explained the RHT-fibers in channel maps as images of PPP cold density filaments (Clark et al. 2019). Thus it is important to put this explanation to the test.

A direct observational test of whether RHT-fibers originate from velocity caustics or cold neutral filaments is presented in Fig. 7. We conducted RHT analyses on the raw channel p , VDA-decomposed velocity contribution map p_v , density contribution map p_d , and FIR intensity map I_{353} . We repeated the RHT analyses using different parameters (see Fig. C1 in Appendix C) to provide the optimal alignment of RHT fibers and magnetic field obtained through polarization observations.

Our results indicated that p_d and I_{353} show a similar appearance

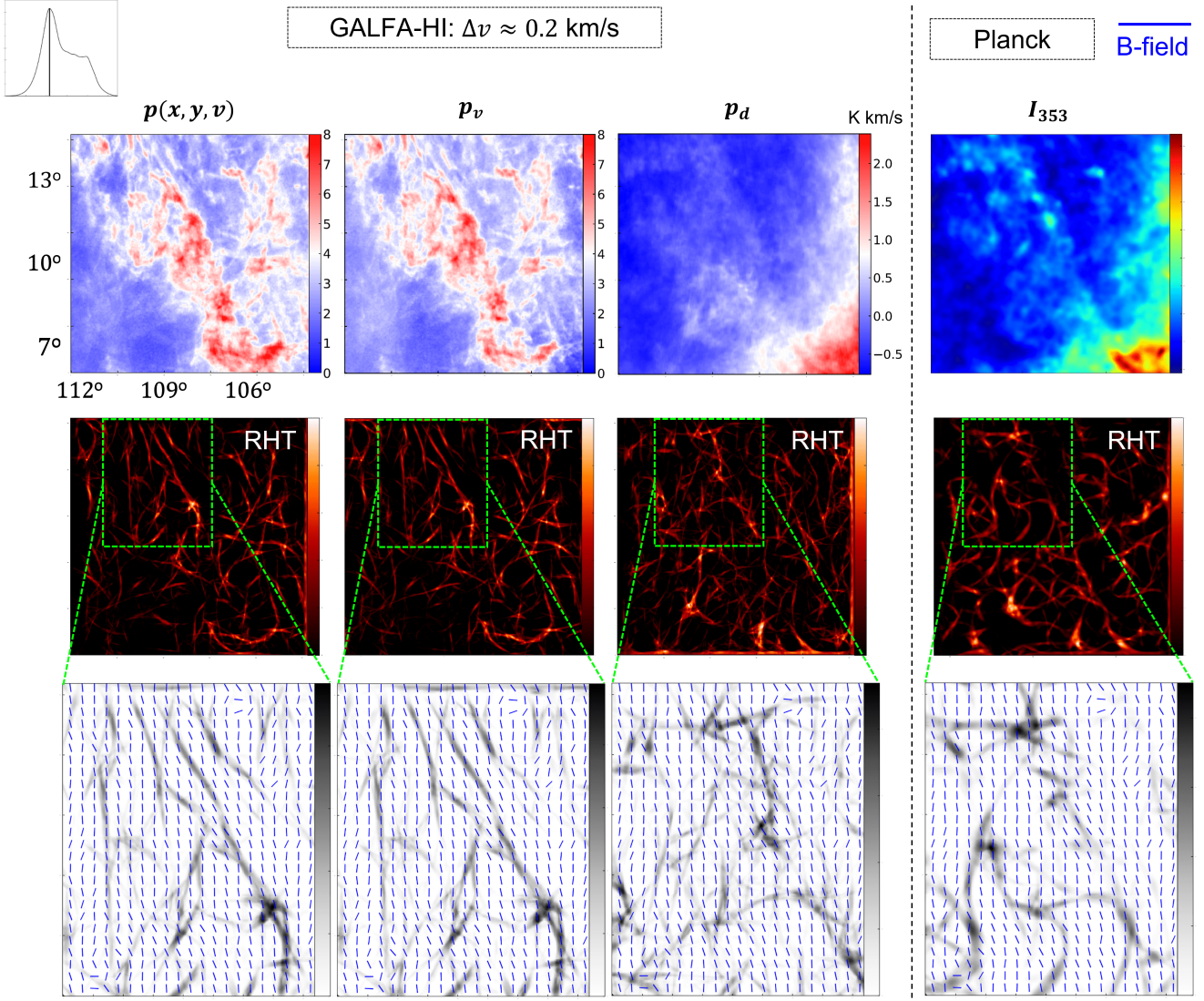


Figure 7. Top: A visual comparison of the thin channel p , density contribution p_d , velocity contribution p_v from GALFA, and Planck 353 GHz FIR intensity map I_{353} . **Middle:** the corresponding RHT-processed maps. **Bottom:** a zoom-in region with RHT-identified fibers overlaid with magnetic field orientation (blue segment) inferred from the Planck 353 GHz polarization. The RHT-identified fibers observed in thin channel maps correspond to velocity caustics represented by p_v , while the density fibers from I_{353} correspond to p_d image and are mostly aligned perpendicular to the magnetic field.

and RHT maps. In contrast, no similarity exists between the thin channel maps p and p_d (also I_{353}) concerning RHT maps. The RHT maps of thin channels p are comparable to the RHT maps of velocity caustics p_v . The perpendicular alignment of RHT-fibers and magnetic fields inferred from Planck 353 GHz polarization is particularly visible in the cases of p_d and I_{353} . Such perpendicular alignment is contributed by the density structures that are perpendicular to the magnetic field (see Fig. 4) and is expected for supersonic compressible MHD turbulence (Xu et al. 2019; Beattie & Federrath 2020). This effect is natural, as shock compression of gas mostly occurs along the magnetic field in the presence of a strong magnetic field, resulting in structures perpendicular to magnetic fields.

Fig. 7 shows that the thin channel map p resembles p_v , which denotes the velocity contribution in p . Their RHT maps are similar and the identified RHT fibers align with magnetic fields. This finding is consistent with the numerical analysis presented in § 4. Further

tests were conducted by altering the channel width and modifying the v_{los} of p in Figs. C2 and C3. All the results confirm that RHT fibers in a thin channel map arise from the velocity caustics effect. Thus, the success of the RHT technique in tracing magnetic fields reported in (Clark et al. 2014, 2015) is due to the alignment of velocity caustics with the magnetic field.

Our study confirms the conclusion from MHD turbulence theory (see Beresnyak & Lazarian 2019), namely, the anisotropy of velocity statistics better traces magnetic field than the anisotropy of density statistics. Thus, it is advantageous to use VDA to remove the density contributions from the data when using RHT to trace the magnetic field.⁶

⁶ In terms of the orientation of filaments, we confirm the density filaments in HI are not different from the density filaments explored in isothermal gas.

6 COMPARISON WITH EARLIER STUDIES

6.1 Motivation for the present study: Theory-based versus empirical approaches

The theory of mapping turbulent gas from PPP to PPV space, as formulated in Lazarian & Pogosyan (2000), predicts that the intensity structures in spectroscopic channel maps, i.e., slices of PPV cubes, can originate from velocity fluctuations, known as velocity caustics. When the channel width is thin, the intensity structures are dominated by velocity caustics, resulting in a shallower power spectrum than of thick channels (Lazarian & Pogosyan 2000; Kandel et al. 2016). The theory's quantitative predictions were numerically tested in several observational data sets, including HI, molecular lines ^{12}CO , ^{13}CO , ^{18}CO , and ion lines [S II], [N II], to study turbulent statistics (Padoan et al. 2006; Swift & Welch 2008; Lazarian 2009; Arthur et al. 2016). The observed changes in the power spectrum of channel maps were consistent with the theoretical expectations. The spectral slopes were utilized to recover the 3D velocity spectrum through the Velocity Channel Analysis (VCA; Lazarian & Pogosyan 2000). The results generally agreed with those obtained through other independent approaches (Armstrong et al. 1995; Chepurnov & Lazarian 2010).

In this study, we provide tests of the velocity caustics using multi-phase HI MHD simulations. The role of (hydrodynamic) turbulence is to induce velocity crowding. On the other hand, the magnetic field introduces anisotropy to the structures, resulting in striations preferentially aligned with the magnetic field. This anisotropy was already discussed by Lazarian et al. (2002); Lazarian & Pogosyan (2012); Kandel et al. (2016) and tested in Esquivel et al. (2015). The anisotropies caused by velocity caustics in thin channel maps can be studied locally by measuring gradients of intensities in channel maps. This resulted in the Velocity Channel Gradient (VChG) technique to trace magnetic field orientation (Lazarian & Yuen 2018a).

Clark et al. (2014) proposed an empirical way of tracing magnetic fields using the linear structures identified by RHT within velocity channel maps. However, Clark et al. (2019) denied the existence of velocity caustics and maintained that the striations identified by RHT as fibers are actual cold-density filaments aligned with the magnetic field. While the arguments raised by Clark et al. (2019) were addressed in Yuen et al. (2019), the controversy about the nature of HI striations continued with Peek & Clark (2019); Kalberla & Haud (2020) in denying the existence of velocity caustics and the very validity of the numerically (Esquivel et al. 2003; Chepurnov & Lazarian 2009; Padoan et al. 2009) and observationally (Lazarian et al. 2002; Lazarian & Pogosyan 2012; Kandel et al. 2016) tested Lazarian & Pogosyan (2000) theory.

The biggest obstacles to achieving a consensus were (1) the difficulties in separating the velocity and density contributions in HI channel maps and (2) the challenges in simulating realistic multi-phase HI gas to provide a direct comparison with the observations. The first problem was recently addressed in Yuen et al. (2021) by introducing the VDA technique to separate velocity and density separation. The paper's HI data analysis complements the present analysis. It also testified to the importance of velocity caustics compared to density filaments. Later, Ho et al. (2021) developed state-of-the-art numerical simulations of magnetized multiphase HI. Based on these developments, we find it appropriate to have an objective discussion of the nature of the striation in HI thin channel maps.

Namely, these filaments are not necessarily aligned parallel to the magnetic field (Hu et al. 2019b; Xu et al. 2019; Beattie & Federrath 2020).

6.2 USM analysis for HI and FIR observations

6.2.1 Un-normalized parameter in USM analysis

Clark et al. (2019) and Kalberla & Haud (2020) argued that the striation seen in the Galactic 21 cm channel maps arises exclusively from actual cold HI density filaments. They compared unsharp masked (USM) HI intensity structures within spectroscopic channels to Planck FIR observations; the latter revealed the projected density. The USM analysis highlights the contrast along the structures' edges, and these edges were expected to be small-scale structures (Kalberla & Kerp 2016). Clark et al. (2019) and Kalberla & Haud (2020) appealed to the (overlapping) correlation between the USM structures and the FIR map as evidence for supporting their explanation that the striations observed in 21 cm channel maps are actual cold HI filaments, but fully denying velocity caustics effects. However, the correlation is quantified by a parameter ΔI_{857} (Clark et al. 2019; see also Appendix A)⁷. The ΔI_{857} 's value of ~ 0.5 – 0.7 reported in Clark et al. (2019) (see their Fig. 6) is un-normalized, which means ΔI_{857} 's upper bound is not unity (see Appendix A). After proper normalization was introduced, this correlation was found to be insignificant (Yuen et al. 2019).

Instead, we utilize a simple approach to quantify the importance of velocity contribution (p_v) and density contribution (p_d) in channel maps (p). We rely on the normalized covariance coefficient (NCC). Our analysis indicates that the velocity contribution is more significant in thin channels (see Fig. 6) where the velocity width (Δv) is less than the velocity dispersion (σ_v). Below we also present a numerical experiment to demonstrate why this USM analysis is inappropriate for testing velocity caustics from a different angle.

6.2.2 USM analysis does not rule out velocity caustics

As illustrated in Fig. 8, we generated a synthetic PPV cube from a density field $\rho(x, y, z)$ and velocity field $v(x, y, z)$. The density field $\rho(x, y, z)$ consists of a two-layer hemisphere with a central high-density (ten times higher than the outskirt) layer and an outskirt low-density layer. At the same time, the LOS velocity component v is adopted from the MHD simulation. This two-layer setup aims to eliminate any pre-existing density structures correlated with the magnetic field and examine the effect of high-density structures, which are typically CNM in observation, on the USM analysis. We see the 3D intensity structures in PPV space are highly distorted and do not resemble the real density hemisphere. The 2D intensity structures within a thin channel become filamentary and anisotropically elongated along the magnetic field direction. These filamentary intensity structures are purely created by velocity caustics. We applied the USM to the thin channel in a similar way to Clark et al. (2019) and Kalberla & Haud (2020). The USM intensity structures are overlaid with the central high-density area of the projected density hemisphere.

Instead of denying the existence of velocity caustics, the correlation of overlapping structures supports its presence. In our numerical experiment, if the velocity caustics effect were insignificant, we should only see two large-scale circles in the channel map, and the USM analysis would output only the circular edges. However, as

⁷ ΔI_{857} is defined as (Clark et al. 2019):

$$\Delta I_{857} = \frac{\langle I_{857} \omega \rangle - \langle I_{857} \rangle \langle \omega \rangle}{\langle \omega \rangle} = \langle I_{857} \rangle \left(\frac{\langle I_{857} \omega \rangle}{\langle I_{857} \rangle \langle \omega \rangle} - 1 \right), \quad (12)$$

where I_{857} is the intensity of Planck 857 GHz dust emission and ω is the USM-measured intensity fluctuations of a given channel with width Δv .

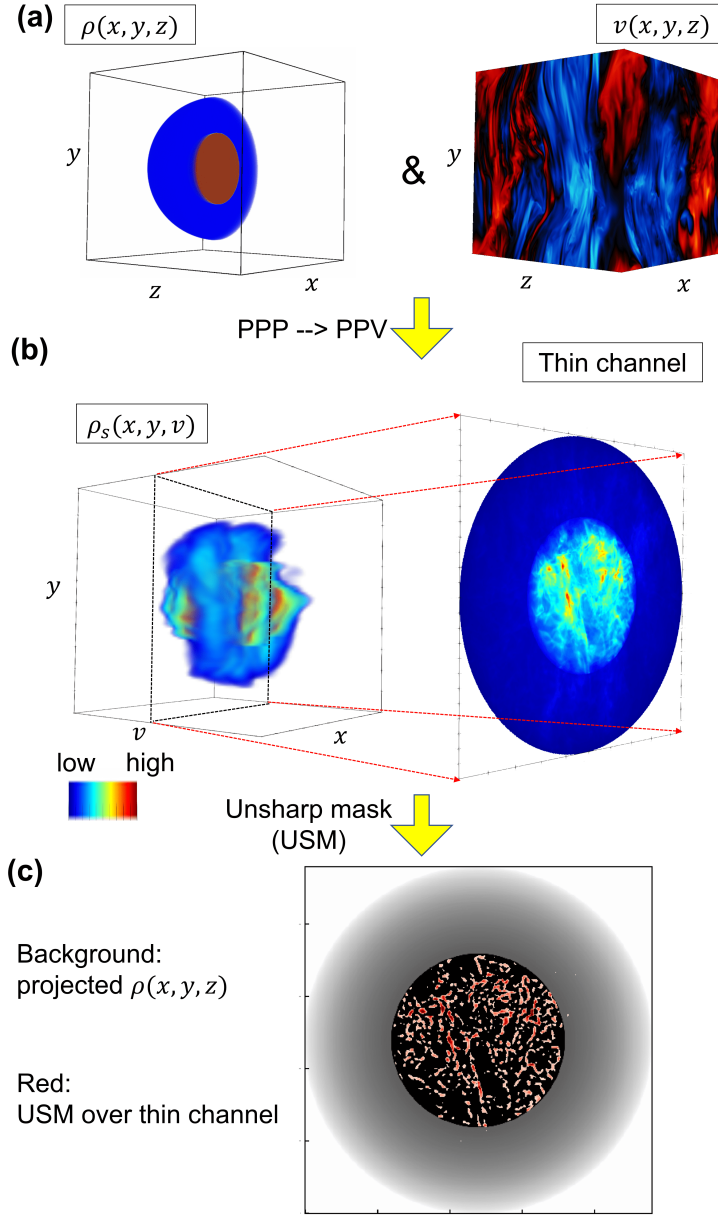


Figure 8. Numerical experiment illustrating the effect of velocity caustics. **Panel (a):** 3D visualization of the input density field $\rho(x, y, z)$ and velocity field's LOS component $v(x, y, z)$ in PPV space. The density field $\rho(x, y, z)$ consists of a two-layer hemisphere with a central constant high-density layer and an outskirts constant low-density layer. At the same time, the LOS velocity component v is adopted from the multiphase simulation. The mean magnetic field is oriented along the y -direction and thermal broadening is included. **Panel (b):** Synthetic PPV cube $\rho_s(x, y, v)$ generated from $\rho(x, y, z)$ and $v(x, y, z)$. A thin channel slice is extracted from the cube and shown on the right. **Panel (c):** Comparison of the projected intensity structures (red) extracted by the USM and the projected real density map (background map: black indicates high density and gray indicates low density).

shown in Fig. 8, the USM highlighted many small-scale intensity structures that are purely the results of velocity caustics.

6.2.3 CNM images are not free from velocity caustics

In a real scenario, CNM is typically denser than UNM and WNM (McKee & Ostriker 1977; Cox & Reynolds 1987; HI4PI Collaboration et al. 2016; Peek et al. 2018). The USM analysis potentially may separate the dense CNM from multi-phase HI. However, CNM is not free from velocity caustics, unless a CNM cloud can be fully mapped into a channel as an entity. The latter requires that the CNM

cloud has a velocity dispersion smaller than the channel width. The median Mach number for CNM was observationally reported as $M_S \sim 3.7$ (Kalberla & Kerp 2016). Assuming the CNM cloud has a typical temperature of 100 K (Ferrière 2001), we can estimate the sound speed is $c_s \approx 1.17$ km/s and corresponding velocity dispersion $\sigma_v = c_s M_S \approx 4.33$ km/s, which agrees with the value for a channel can be considered as thin (Stanimirović & Lazarian 2001), as well as our results in Fig. 5. When the channel width is smaller than this typical value, the CNM cloud is also affected by the velocity caustics. For instance, as we see in Fig. 8, the high-constant-density hemisphere is strongly distorted after mapping into PPV space. The correlation

between USM structures and the projected high-density area arises purely from velocity caustics. This agrees with the picture proposed in Yuen et al. (2021) that while fluctuations in the column density can arise from large scales density fluctuations (corresponding to the central high-density circular area in Fig. 8), small-scale intensity structures are still dominated by velocity caustics (corresponding to the USM-structures in Fig. 8).

On the other hand, when CNM is mapped into PPV space, it is distributed into different velocity channels due to the velocity caustics effect. This effect does not mean that CNM disappears in the PPV space or that its position on the POS can be different. The correlation always exists when stacking the FIR map with the channels' high-intensity structures (see Fig. 8). Therefore, the observed correlation between the USM-analyzed HI intensity structures within channels and Planck FIR observations cannot distinguish velocity caustics. Similar to the USM analysis, Peek & Clark (2019) and Murray et al. (2020) tried to examine the velocity caustics by comparing the HI intensity structures with the projected location of quasars and column density, respectively. However, for the same reasons mentioned above, these analyses of stacking projected quantity with the HI intensity structures are inappropriate.

6.2.4 FIR structures are not always parallel to magnetic field

Large-scale density structures also tend to follow the magnetic field in globally subsonic conditions (Xu et al. 2019). This very likely happened in the high-latitude $b > 30^\circ$ regions selected in earlier studies (Clark et al. 2019; Peek & Clark 2019; Kalberla & Haud 2020; Murray et al. 2020; Kalberla & Haud 2023). In Fig. 9, we overlay the magnetic field orientation (inferred from Planck polarization) on the Planck 353 GHz FIR map for a different high-latitude region. Clearly, the FIR density structures are perpendicular to the magnetic field, rather than parallel. These perpendicular FIR structures are ignored in previous studies (Clark et al. 2019; Kalberla & Haud 2020).

Nevertheless, our analysis was performed for three regions, including high-latitude and low-latitude, to give conclusions (see Figs. 5 and D1). Moreover, we noticed the (i) significance of density contribution can increase in low-latitude HI clouds close to the Galactic disk (see Fig. D1); (ii) cold HI in our Galaxy concentrates more on the low-latitude ($|b| < 30^\circ$) regions (see Fig. 9 in Kalberla & Haud 2018). A better alignment of striations and magnetic field should be expected in low-latitude regions if the cold-filament explanation is true⁸.

In short, Clark et al. (2019); Kalberla & Haud (2020, 2023) did not take into account the velocity caustics effect and interpreted those small-scale intensity fluctuations as real cold density filaments. These studies conflict with our numerical experiment and observational evidence which yield the following: (1) the FIR-HI correlation observed through the use of the USM can indeed be generated by velocity caustics (see Fig. 8), while real small-scale density structures can also be

⁸ We would like to note that the use of the USM analysis may pose challenges in low-latitude regions due to the mixing of numerous HI clouds along the LOS. However, as an alternative approach, the magnetic field traced by RHT-fibers should remain unaffected by the mixing, provided that the cold filament explanation is correct. In this scenario, we should expect to observe an improved agreement between the RHT-traced magnetic field and Planck results in low-latitude regions, as well as a positive correlation with channel width. Specifically, a better alignment is expected for the cold filament explanation, when using only thick channels ($\Delta v > \sigma_v$) rather than only thin channels or a mix of thick and thin channels, as such thick channels are certainly dominated by density.

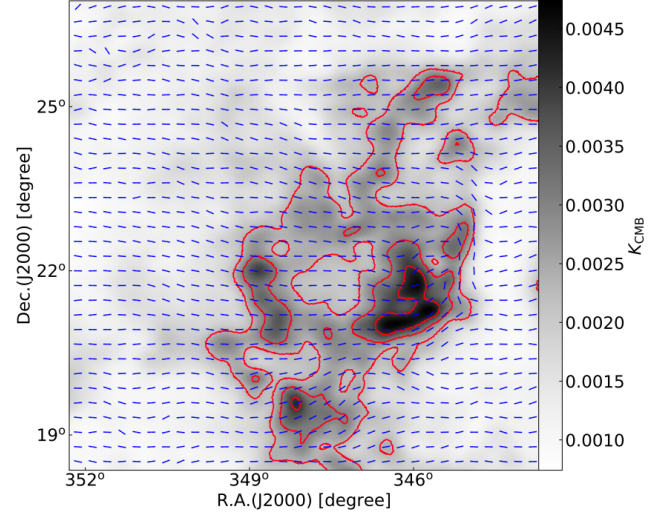


Figure 9. Magnetic field orientation (blue segment) overlaid with the Planck 353 GHz FIR map (background). The red contours start from 0.0023, 0.003, 0.004 K_{CMB} .

present. Thus, the corresponding FIR-HI correlation is not capable to distinguish between structures created by velocity caustics and real density structures within thin channels. (2) The FIR structures do not always align with magnetic fields (see Figs. 7 and 9). A good parallel alignment is observed in specific regions (Clark et al. 2015, 2019) with $b > 30^\circ$, where tangling of the magnetic field along the LOS is not as significant as in the direction towards the Galactic disk.

6.3 Comparison of numerical simulations

Some reported results that allegedly contradicted the caustic-based interpretation of the observed striations were obtained using low-resolution simulations (Clark et al. 2019). In the numerical experiment by Clark et al. (2019), 128^3 isothermal simulations were conducted using the RAMSES code (Teyssier 2002) for hydrodynamic turbulence, without accounting for the complexity of the actual ISM (Armstrong et al. 1995; Chepurnov & Lazarian 2010; Crutcher 2012; Planck Collaboration et al. 2015; Ha et al. 2022). Further general concerns over the limited inertial range and dynamical range in simulations were raised by Kalberla et al. (2022), so a convergence study is necessary for this scenario.

To address the limitations, we included high-resolution isothermal MHD simulation with 792^3 cells, for comparison purposes (see Figs. B1 and Fig. B2). Our numerical results indicate that velocity caustics are essential and the thermal broadening effect is minimum, especially in the supersonic case, consistent with theoretical expectations (Lazarian & Pogosyan 2000). Another high-resolution study (480^3 to 1200^3) in Yuen et al. (2021) supports our findings.

Furthermore, the multi-phase nature of HI was the main argument in Clark et al. (2019) against interpreting striations in terms of velocity caustics, since the theoretical works by Lazarian & Pogosyan (2000) and others mainly dealt with turbulence in single-phase media. To address this concern, we included non-scale-free multi-phase simulations with 480^3 cells in our current study. Our results are consistent with the caustic interpretation of the observed channel map striation. Especially, another multi-phase numerical study in Gong et al. (2023) also finds the cold-density filament can be perpendicular to the magnetic field (see Fig. 10 in Gong et al. 2023). In contrast, no

numerical convergence study or multi-phase simulations have been carried out to support the cold-filament interpretation (i.e., cold-filaments always parallel to the magnetic fields) proposed by [Clark et al. \(2019\)](#).

7 DISCUSSION

7.1 Origin of HI striations in thin channels

This study investigates the origin of elongated HI intensity structures within thin channels through a comprehensive set of numerical simulations, including isothermal MHD and multi-phase conditions. These simulations allow us to separate the various physical mechanisms involved. Our isothermal simulations reveal that the velocity caustics effect dominantly creates filamentary intensity structures within thin channels (see Fig. B1). The velocity caustics also inherit the anisotropy of MHD turbulence, so these structures become aligned parallel to the magnetic fields. The phase transition between CNM, UNM, and WNM has no negative effect on the alignment (see Fig. 3). This observation is also supported by the analysis of GALFA-HI clouds, where we demonstrate that, when the channel width is thin, the HI channel is dominated by velocity contribution (see Fig. 7).

We have noticed that the preference for the cold-filament interpretation ([Clark et al. 2019](#)) may stem from a misconception about turbulence. For example, [Kalberla et al. \(2022\)](#) have pointed out that [Clark \(2018\)](#) and [Clark et al. \(2021\)](#) have demonstrated that HI striations are coherent structures, but [Kalberla et al. \(2022\)](#) and [Kalberla & Haud \(2023\)](#) also claimed that turbulence cannot be invoked to generate coherent structures because they expect turbulence to be a purely random process. However, it is important to note that turbulence is not entirely random. In fact, turbulence is highly structured and can exhibit a wide range of coherent and self-organizing patterns ([Tsinover & Levich 1983](#); [Fiedler 1988](#); [McComb 1990](#)). The reason for this confusion lies in the complex interactions between fluid elements that occur within a turbulent flow. These interactions can produce intricate patterns of vortices, eddies, and waves that evolve in a self-similar and fractal-like manner over a wide range of scales. Our 3D visualization of the velocity field and density field in a turbulent box (see Figs. 8 and 4) clearly shows coherent structures. This was also evident in a number of studies ([Saffman 1981](#); [Tsinover & Levich 1983](#); [Fiedler 1988](#); [Burkhart et al. 2009](#); [Federrath 2013](#); [Chong et al. 2015](#); [Xu et al. 2019](#); [Beattie & Federrath 2020](#); [Ferrand et al. 2020](#); [Krieger et al. 2020](#); [Vlahos & Islikier 2023](#)), the largest 10048³-cell turbulence simulation ([Federrath et al. 2021](#)), and in-situ solar wind measurements of turbulence ([Mangeney et al. 2014](#); [Perrone et al. 2015](#); [Sondhiya et al. 2016](#); [Khabarova 2017](#)). One can refer to the literature "Coherent structures in turbulent flows" ([Fiedler 1988](#)), "Statistical Fluid Mechanics, Volume II: Mechanics of Turbulence" ([Monin & Yaglom 2013](#)), and recent "Formation and Evolution of Coherent Structures in 3D Strongly Turbulent Magnetized Plasmas" ([Vlahos & Islikier 2023](#)).

It should be noted that the striations in thin channels and real density filaments are different. Our study does not exclude the possibility that real density filaments, especially low-density filaments, can align with magnetic fields in PPP space. We are seeking to answer the origin of HI striations in thin channels and conclude that velocity caustics cannot be ignored.

7.2 Density filaments versus spectroscopic striations

The formation of density filaments is essential in understanding the ISM ([Molinari et al. 2010](#); [André et al. 2010](#); [Ho et al. 2023](#)). Since Herschel space telescope observations of molecular clouds revealed filamentary patterns of the ISM, several filament-detection algorithms have been proposed ([Men'shchikov 2013](#); [Juvela 2016](#); [Alina et al. 2022a](#)). These continuum observations contain only density information bringing new insights about, in particular, the star formation process ([Panopoulou et al. 2022](#); [André et al. 2022](#)). The situation, however, is more complicated in HI spectroscopic observations. Instead, velocity caustics raised by the spectroscopic mapping from PPP to PPV space can create virtual intensity striations. These striations do not exist in real space but dominate the intensity structures in thin channels (see Fig. 2).

The velocity caustics create striations that imprint velocity statistics, while real density filaments contain only density information. Therefore, their properties differ significantly. For velocity statistics, MHD turbulence creates anisotropic velocity structures elongated along magnetic fields ([Brandenburg & Lazarian 2013](#); [Beresnyak & Lazarian 2019](#)), which has been observed in numerical simulations ([Montgomery & Turner 1981](#); [Shebalin et al. 1983](#); [Federrath 2016](#); [Tritsis et al. 2018](#); [Beattie & Federrath 2020](#)) and explained by MHD and turbulent reconnection theory ([Goldreich & Sridhar 1995](#); [Lazarian & Vishniac 1999](#)). Subsequent numerical studies have confirmed these findings ([Cho & Vishniac 2000](#); [Maron & Goldreich 2001](#); [Cho & Lazarian 2003](#); [Kowal et al. 2009](#)). On the other hand, the behavior of the density field is more complex. Low-density structures can follow velocity statistics ([Beresnyak et al. 2005](#)), while shocks tend to create high-density filaments perpendicular to the magnetic field ([Planck Collaboration et al. 2016](#); [Xu et al. 2019](#); [Beattie & Federrath 2020](#)). The thermal instability in HI would increase compressibility and make the formation of perpendicular filaments more vivid. Therefore, when density contribution dominates the thin channels, perpendicular and parallel alignments should be present between the channel's intensity structures and magnetic fields. In contrast, only parallel alignment is expected to be prominent in the case of velocity dominance.

Our 3D visualization of the multi-phase simulation's density and magnetic fields in Fig. 4 confirms that real high-density filaments can be perpendicular to magnetic fields (see also Fig. 10 in [Gong et al. 2023](#)). This is also observed in the Planck FIR map (see Fig. 9). We identified RHT-fibers for the thin channel maps and found that the perpendicular density filaments seen in PPP space have a marginal contribution to the thin channel RHT-fibers. The RHT-fibers are preferentially aligned along the magnetic field direction, similar to what is observed in GALFA-HI data (see Fig. 7). This suggests that striations in thin channels mainly arise from velocity caustics and not from density filaments. Therefore, it is important to correctly interpret the results with velocity statistics when using thin channels, particularly in studies aiming to trace Galactic magnetic fields ([Ma et al. 2023](#); [Campbell et al. 2022](#); [Kalberla & Haud 2023](#)).

7.3 Implications for HI Related Studies

7.3.1 HI striations detected with the Rolling Hough Transform

We demonstrate that the elongated HI intensity structures within thin channels, and the corresponding RHT-detected fibers, originate from the velocity caustics effect. The properties of the RHT-fibers in thin channels should be dominated by velocity statistics rather than density statistics. On the other hand, the RHT-fibers in thick channels contain more density information. However, density structures are

less reliable tracers of magnetic fields because high-density structures can be perpendicular to the magnetic fields (see [Planck Collaboration et al. 2016](#); [Alina et al. 2019](#); [Xu et al. 2019](#); [Beattie & Federrath 2020](#) and Fig. 9). Therefore, caution should be exercised when using RHT-based polarization studies ([Clark et al. 2014, 2015](#); [Clark 2018](#); [Clark & Hensley 2019](#)) that have completely ignored the velocity caustics effect or have not distinguished between thick ($\Delta v > \sigma_v$) and thin channels ($\Delta v < \sigma_v$). For example, [Alina et al. \(2023\)](#) found that the orientation of the filamentary HI structures in the Milky Way toward the Large Magellanic Cloud disagrees with the polarization of foreground stars. Since turbulence and HI are important factors in modeling Galactic foreground polarization, it is essential to correctly interpret the underlying turbulence physics based on either velocity or density (a bad tracer of magnetic fields in HI compared to velocity, due to the presence of perpendicular filaments, see Figs. 4 and 9 in this work and Fig. 10 in [Gong et al. 2023](#)). Therefore, physical interpretations that do not consider velocity statistics require careful revision ([Clark et al. 2015](#); [Clark & Hensley 2019](#); [Clark 2018](#); [Clark et al. 2021](#)).

Furthermore, the outputs of most filament-detection algorithms heavily rely on user-dependent parameters, leading to bias ([Green et al. 2017](#)). Thus, retrieving the magnetic field's direction from the filament orientation can be uncertain due to parametrization. This parametrization issue can in principle be tackled with a machine learning-based approach (e.g., [Alina et al. 2022a](#)). We provide an example of the parameter dependence of the output maps using the RHT method in Appendix C.

7.3.2 Magnetic fields traced with Velocity Channel Gradients

Velocity Channel Gradients (VChGs; [Lazarian & Yuen 2018a](#)) was developed as a new technique to trace the magnetic fields based on the velocity statistics in thin channels' striations. Its theoretical foundation was questioned by [Clark et al. \(2019\)](#), but this work, as well as other studies ([Yuen et al. 2019, 2021](#)), has proven the validity of velocity caustics in thin channels. VChGs advantageously holds the promise of obtaining the 3D distribution of the Galactic magnetic fields, including both orientation and strength ([Hu & Lazarian 2023a](#)).

VChGs is a part of the more general Velocity Gradient Technique (VGT; [González-Casanova & Lazarian 2017](#); [Yuen & Lazarian 2017](#); [Lazarian & Yuen 2018a](#); [Hu et al. 2018](#)). VGT can also employ velocities centroids (i.e., moment-1 map or even higher order) to trace the magnetic fields ([Hu et al. 2020d](#)). Compared to the centroid-based method, VChGs calculated from thin channels are dominated by velocity statistics with less contamination by density, making VChGs a major tool of the VGT. In its turn, VGT is a part of the Gradient Technique (GT) that employs general properties of MHD turbulence for tracing magnetic fields and measuring their strength. The GT has been applied to synchrotron intensity data emissions ([Lazarian et al. 2017](#); [Lazarian & Yuen 2018b](#); [Hu et al. 2020c](#)), Faraday rotation map ([Lazarian & Yuen 2018b](#)), X-ray measurements ([Hu et al. 2020c](#)), and near-infrared observations ([Hu et al. 2022a](#)). The comparison of the results with the available polarization data was successful. The theoretical foundation of all these branches of GT is the anisotropic MHD turbulence⁹.

⁹ At low M_S the density acts as a passive scalar copying the statistics of velocities ([Monin & Yaglom 2013](#)).

7.3.3 VChGs and RHT: Comparison and synergy

RHT is a technique designed to identify filamentary structures in images ([Clark et al. 2014](#)), while VChGs is a technique to trace magnetic field direction and obtain their magnetization ([Lazarian & Yuen 2018a](#); [Lazarian et al. 2018](#)). RHT was employed in [Clark et al. \(2015\)](#) and subsequent studies to trace magnetic fields using spectroscopic channel maps ([Clark 2018](#); [Clark & Hensley 2019](#); [Clark et al. 2021](#)). They interpreted the results based on density statistics. However, in this paper, we have shown that the fibers observed with RHT mostly arise from velocity caustics.

VChGs' accuracy in single-phase media has been widely tested using numerical simulations and observations ([Lazarian & Yuen 2018a](#); [Hu et al. 2019a](#); [Alina et al. 2022b](#); [Hu et al. 2022a](#); [Liu et al. 2022](#); [Tram et al. 2022](#); [Hu et al. 2022c](#); [Schmaltz et al. 2022](#)). The dominance of velocity caustics in cold species with insignificant thermal broadening is robustly true. Although thermal broadening can be significant and phase transition can happen in multi-phase HI, our study with comprehensive numerical and observational tests confirms that the velocity caustics still dominate multi-phase HI thin channels. The theoretical foundation of VGT is justified, and the corresponding multi-phase numerical test for VGT is given in [Ho & Lazarian \(2023\)](#).

From the technical point of view, VChGs is a robust technique that does not require adjustable parameters. VChGs' well-understood theoretical foundations, which stem from MHD turbulence theory ([Goldreich & Sridhar 1995](#); [Lazarian & Vishniac 1999](#)) and spectroscopic mapping theory ([Lazarian & Pogosyan 2000](#)), enable its application to various physical environments. This is achieved by isolating the contributions of density fluctuations, rendering it less susceptible to variations in the orientation of density features ([Hu et al. 2018](#); [Lazarian & Yuen 2018a](#)); removing parasitic contributions of fast MHD modes ([Ho & Lazarian 2021](#)); and gauging its accuracy in the presence of non-turbulent (i.e., inflow, outflow, and differential rotation) velocity fields ([Hu et al. 2020a, 2022a,c](#)).

Our study shows that VChGs compared to RHT, provide higher accuracy of magnetic field testing (see Fig. E1 in Appendix E). In addition, the distribution of VChGs orientation within an elementary sub-block provides the value of magnetization M_A^{-1} (see [Lazarian et al. 2018](#), and Fig. E3 in Appendix E), which can then be used to obtain magnetic field strength using the approach in [Lazarian et al. \(2020\)](#); [Hu & Lazarian \(2023a\)](#). No such capabilities have been reported for the RHT application to channel maps. RHT is one of the ways of identifying filamentary structures that can be successfully employed for its primary purpose once the usage of input parameters is justified (see Appendix C, Fig. C1).

7.3.4 VChGs and Machine Learning

Machine learning (ML) is a rapidly growing field in astrophysics that holds promise for tracing magnetic fields using spectroscopic maps ([Xu et al. 2023](#)). However, it is crucial to understand the reasons for the feasibility of such mapping with ML and to be aware of potential pitfalls.

A recent study combined ML learning with velocity gradient in Taurus ([Xu et al. 2023](#)), although the authors did not employ the latest modifications of VChGs, making it challenging to make quantitative comparisons. Magnetic field tracing and other areas of observational data analysis can benefit from the ML approach. However, it is vital to comprehend the physical foundation of the applied procedures while utilizing ML. This paper clarifies the connection between striations observed in channel maps and velocity fluctuations aligned by the

magnetic field, providing a justification for obtaining magnetic field maps through the ML approach. The space-velocity mapping theory (Lazarian & Pogosyan 2000; Kandel et al. 2016) can help avoid the pitfalls of the brute force ML approach.

The striations observed in thin spectroscopic channels, as shown in this work, are correlated with MHD turbulence (Lazarian & Pogosyan 2000; Lazarian & Yuen 2018a). The ML approach can be further improved and extended by taking into account the theoretical predictions that the VChGs' amplitude (Yuen & Lazarian 2020a) and curvature (Yuen & Lazarian 2020b) are correlated with M_S and M_A , respectively.

7.3.5 Obtaining Magnetic field strength using HI data

The Davis–Chandrasekhar–Fermi (DCF) method (Davis 1951; Chandrasekhar & Fermi 1953) is commonly used to estimate the POS magnetic field strength in ISM (Hu et al. 2021; Pattle et al. 2021; Hwang et al. 2021; Li et al. 2021; Hoang et al. 2022; Tram et al. 2022; Kalberla & Haud 2023). By assuming magnetic field fluctuations δB are fully raised by velocity fluctuations σ_v of Alfvénic turbulence, the mean POS magnetic field can be approximately obtained from:

$$B \approx f \frac{\sqrt{4\pi\rho\sigma_v}}{\delta\phi_B}, \quad (13)$$

here $f \approx 0.5$ is a correction factor (Ostriker et al. 2001), ρ is gas mass density, σ_v is velocity dispersion, and $\delta\phi_B$ is the dispersion of magnetic field orientation. The crucial term in DCF, as well as its modifications (Heitsch et al. 2001; Falceta-Gonçalves et al. 2008; Skalidis et al. 2021; Chen et al. 2022), is the ratio of σ_v and $\delta\phi_B$.

For observational implementation, σ_v is typically estimated from line width, while $\delta\phi_B$ can be obtained from polarization measurements (Pattle et al. 2021; Hu et al. 2021; Hwang et al. 2021; Li et al. 2021; Hoang et al. 2022; Tram et al. 2022; Chen et al. 2022). It is crucial for the correct implementation of DCF that $\delta\phi_B$ invoked in the turbulent dynamo process is on the same scale as σ_v (Moffatt 1978; Schekochihin et al. 2004; Brandenburg & Subramanian 2005; Xu & Lazarian 2016). This approach to obtaining $\delta\phi_B$ and σ_v might overestimate B when the regions under study are only small patches of the cloud (Lazarian et al. 2020; Hu & Lazarian 2023a). The overestimation arises from the fact that (i) σ_v estimated from line width corresponds to the velocity fluctuation at injection scale L_{inj} due to the lack of spatial information along the LOS (see Appendix A in Hu & Lazarian 2023b), but (ii) the $\delta\phi_B$ for a small patch with size l corresponds to the fluctuation at scale l . Compared to the angle dispersion for the entire cloud (i.e., at turbulence injection scale L_{inj}), the dispersion for a small patch is reduced by a factor of $\sim (l/L_{\text{inj}})^{1/3}$, assuming Kolmogorov-type turbulence.

Recently, Kalberla & Haud (2023) employed the DCF method and its modifications to estimate the POS magnetic field strength in HI striations using thin channels. For this purpose, $\delta\phi_B$ is calculated from the HI-striation-based magnetic field tracing method (Kalberla et al. 2021) and σ_v is estimated from HI line width. Firstly, the HI striations are assumed to be real density filaments in Kalberla & Haud (2023), which, however, has been proven not to be the case. Secondly, the $\delta\phi_B$ is calculated at an angular scale of $18'$ (see Sec. 5.1 in Kalberla & Haud 2023). This corresponds to a length scale of $l \sim 0.5$ pc or $l \sim 1.3$ pc for their different assumptions of HI LOS distance of 100 pc or 250 pc, respectively. This length scale is much smaller than the typical turbulence injection scale $L_{\text{inj}} \sim 100$ pc in the ISM (Armstrong et al. 1995; Chepurnov & Lazarian 2010; Ha

et al. 2022), leading to a significant overestimation of magnetic field strength.

On the other hand, Lazarian et al. (2020) suggested the use of sonic and Alfvén Mach numbers to obtain the magnetic field strength. This approach mitigated the overestimation in the DCF method¹⁰. A successful application of such an approach to HI is given by Hu & Lazarian (2023a).

7.3.6 Velocity Channel Analysis

Velocity Channel Analysis (VCA) was proposed in Lazarian & Pogosyan (2000) to analyze intensity statistics in PPV spectroscopic data and retrieve the underlying 3D spectra of velocities and densities. The significance of velocity caustics is correlated with the channel map's width, as shown in Fig. 2, and the channel's intensity statistics vary accordingly, which is imprinted in the channel's power spectrum. Lazarian & Pogosyan (2000) formulated the correlation between the channel's spectrum and velocity and density power spectra, enabling one to determine the spectral index of the velocity and density power spectra through VCA analysis.

Specifically, thin channels' power spectrum is shallower than thick channels due to the intense small-scale striations created by velocity caustics Lazarian & Pogosyan (2000). However, Clark et al. (2019) challenged this interpretation and questioned the applicability of VCA to multiphase HI, favoring instead that small-scale CNM structures are responsible for the observed HI striations and the corresponding shallow power spectrum. This interpretation conflicts with observational results, as shown by Kalberla & Haud (2020), who decomposed CNM from the Effelsberg Bonn HI Survey (EBHIS) observations and demonstrated that CNM's spectra are steep in the case of thin channels, suggesting small-scale CNMs are rare in thin channels compared to those in thick channels.

On the other hand, VCA has been successfully applied to both single-phase species and multi-phase HI by different groups (see Tab. 5 in Lazarian 2009, Fig. 1 in Padoan et al. 2006, Fig. 18 in Swift & Welch 2008, and Fig. 1 in Arthur et al. 2016). The numerical and observational analysis presented in this paper further demonstrates that the velocity crowding effect is significant for thin channel maps and is responsible for a significant portion of intensity fluctuations in the channel maps. These results support the applicability of VCA to both single-phase species and multi-phase HI.

8 SUMMARY

It is well known that intensity fluctuations observed in PPV can arise from actual density fluctuations and the effect of velocity crowding. The latter is the effect that cannot be ignored while analyzing fluctuations in PPV space in general and velocity channel maps in particular. Magnetized turbulence is anisotropic and affects the intensity fluctuations observed in channel maps. The relative role of densities and velocities for the striation observed in thin 21 cm channel maps is explored in this paper. For this purpose, we use synthetic maps of the multi-phase simulations of magnetized HI and compare the results with theoretical expectations and GALFA HI maps.

To better separate the density and velocity contributions, we apply

¹⁰ In addition, the problem with using the smaller patches of data can be mitigated by using the Differential Measure Analysis (DMA) that employs local structure-function for measuring the dispersion (Lazarian et al. 2022; Hu & Lazarian 2022).

to both synthetic and GALFA HI maps a new statistical tool, Velocity Decomposition Algorithm (VDA), and compare the results obtained with this tool to the input velocity channel maps available. Our major findings are as follows:

(i) Our analysis of both synthetic maps obtained with multi-phase HI simulations and GALFA HI observations testifies that it is incorrect to disregard the contribution from velocity caustics to the intensity fluctuations in thin channel maps. In fact, we demonstrate that the velocity caustics dominate the striations observed in thin 21 cm velocity channel maps.

(ii) Our study demonstrates the ability of VDA to distinguish between the contribution from velocity caustics and density filaments to the striation observed in thin channel maps obtained with multi-phase HI simulations.

(iii) We demonstrate that the VDA-decomposed velocity maps strongly correlate with the original thin channel maps and do not correlate with the column density maps representing density filaments. Applying the VDA analysis to a GALFA-HI cloud reveals that the HI thin channel maps with $\Delta v \approx 0.2$ and 4 km/s are primarily dominated by prominent velocity caustics.

(iv) We show that the arguments supporting interpreting striation observed in thin channel maps as arising from the projection of density filaments to the PPV space are not tenable. For instance, the correlation between unsharp-masked HI structures and far infrared emission is not an argument to disregard the velocity caustics effect.

(v) We confirm that the fibers detected by filament-detection algorithms, such as the RHT, within HI thin channels arise from velocity caustics rather than real density structures. The studies that derive magnetic field orientation and strength employing intensity filaments observed in thin channel maps should be revised to account for the velocity origin of the structures.

(vi) We show that real HI and FIR density structures can align both parallel or perpendicular with magnetic fields, which correspond well to the numerical simulations. On the contrary, the striation arising from velocity caustics is mostly aligned parallel to the magnetic field. The latter corresponds both to the expectations based on theory and numerical simulations. This makes the striation a reliable way to study magnetic fields.

(vii) Our study provides additional evidence that in combination with VDA, VCA can be applied to study turbulence spectra in HI. We also prove that VChGs can successfully trace magnetic fields in HI.

ACKNOWLEDGEMENTS

We thank Ka Ho Yuen and Blakesley Burkhart for the helpful discussions. Y.H. and A.L. acknowledge the support of NASA ATP AAH7546 and ALMA SOSPADA-016. Financial support for this work was provided by NASA through award 09_0231 issued by the Universities Space Research Association, Inc. (USRA). This work used SDSC Expanse CPU at SDSC through allocation PHY230032 from the Advanced Cyberinfrastructure Coordination Ecosystem: Services & Support (ACCESS) program, which is supported by National Science Foundation grants #2138259, #2138286, #2138307, #2137603, and #2138296. DA acknowledges the Nazarbayev University Faculty Development Competitive Research Grant Program #11022021FD2912. D.P. thanks KITP, University of Santa-Barbara for hospitality during COSMICWEB23 program and acknowledges that this research was supported in part by the National Science Foundation under Grant No. NSF PHY-1748958.

DATA AVAILABILITY

The data underlying this article will be shared on reasonable request to the corresponding author.

REFERENCES

- Alina D., Ristorcelli I., Montier L., Abdikamalov E., Juvela M., Ferrière K., Bernard J. P., Micelotta E. R., 2019, *MNRAS*, **485**, 2825
- Alina D., Shomanov A., Baimukhametova S., 2022a, *IEEE Access*, **10**, 74472
- Alina D., et al., 2022b, *A&A*, **658**, A90
- Alina D., Bernard J. P., Yuen K. H., Lazarian A., Hughes A., Iskakova M., Akimkhan A., Mukanova A., 2023, *MNRAS*, **518**, 4466
- Andersson B. G., Lazarian A., Vaillancourt J. E., 2015, *ARA&A*, **53**, 501
- André P., et al., 2010, *A&A*, **518**, L102
- André P. J., Palmeirim P., Arzoumanian D., 2022, *A&A*, **667**, L1
- Armstrong J. W., Rickett B. J., Spangler S. R., 1995, *ApJ*, **443**, 209
- Arthur S. J., Medina S. N. X., Henney W. J., 2016, *MNRAS*, **463**, 2864
- Beattie J. R., Federrath C., 2020, *MNRAS*, **492**, 668
- Beattie J. R., Mocz P., Federrath C., Klessen R. S., 2021, *MNRAS*, **504**, 4354
- Beresnyak A., Lazarian A., 2019, Turbulence in Magnetohydrodynamics
- Beresnyak A., Lazarian A., Cho J., 2005, *ApJ*, **624**, L93
- Brandenburg A., Lazarian A., 2013, *Space Sci. Rev.*, **178**, 163
- Brandenburg A., Subramanian K., 2005, *Phys. Rep.*, **417**, 1
- Burkhart B., Falceta-Gonçalves D., Kowal G., Lazarian A., 2009, *ApJ*, **693**, 250
- Campbell J. L., et al., 2022, *ApJ*, **927**, 49
- Chandrasekhar S., Fermi E., 1953, *ApJ*, **118**, 113
- Chen C.-Y., Li Z.-Y., Mazzei R. R., Park J., Fissel L. M., Chen M. C. Y., Klein R. I., Li P. S., 2022, *MNRAS*, **514**, 1575
- Chepurnov A., Lazarian A., 2009, *ApJ*, **693**, 1074
- Chepurnov A., Lazarian A., 2010, *ApJ*, **710**, 853
- Cho J., Lazarian A., 2003, *MNRAS*, **345**, 325
- Cho J., Vishniac E. T., 2000, *ApJ*, **539**, 273
- Chong K. L., Huang S.-D., Kaczorowski M., Xia K.-Q., 2015, *Phys. Rev. Lett.*, **115**, 264503
- Clark S. E., 2018, *ApJ*, **857**, L10
- Clark S. E., Hensley B. S., 2019, *ApJ*, **887**, 136
- Clark S. E., Peek J. E. G., Putman M. E., 2014, *ApJ*, **789**, 82
- Clark S. E., Hill J. C., Peek J. E. G., Putman M. E., Babler B. L., 2015, *Phys. Rev. Lett.*, **115**, 241302
- Clark S. E., Peek J. E. G., Miville-Deschênes M. A., 2019, *ApJ*, **874**, 171
- Clark S. E., Kim C.-G., Hill J. C., Hensley B. S., 2021, *ApJ*, **919**, 53
- Cox D. P., Reynolds R. J., 1987, *ARA&A*, **25**, 303
- Crutcher R. M., 2012, *ARA&A*, **50**, 29
- Davis L., 1951, *Physical Review*, **81**, 890
- Dickey J. M., Lockman F. J., 1990, *ARA&A*, **28**, 215
- Diemand J., Kuhlen M., Madau P., 2007, *ApJ*, **657**, 262
- Elmegreen B. G., Scalo J., 2004, *ARA&A*, **42**, 211
- Esquivel A., Lazarian A., Pogosyan D., Cho J., 2003, *MNRAS*, **342**, 325
- Esquivel A., Lazarian A., Pogosyan D., 2015, *ApJ*, **814**, 77
- Falceta-Gonçalves D., Lazarian A., Kowal G., 2008, *ApJ*, **679**, 537
- Federrath C., 2013, *MNRAS*, **436**, 1245
- Federrath C., 2016, *Journal of Plasma Physics*, **82**, 535820601
- Federrath C., Klessen R. S., Iapichino L., Beattie J. R., 2021, *Nature Astronomy*, **5**, 365
- Ferrand R., Galtier S., Sahraoui F., Federrath C., 2020, *ApJ*, **904**, 160
- Ferrière K. M., 2001, *Reviews of Modern Physics*, **73**, 1031
- Fiedler H. E., 1988, *Progress in Aerospace Sciences*, **25**, 231
- Goldreich P., Sridhar S., 1995, *ApJ*, **438**, 763
- Gong M., et al., 2023, *arXiv e-prints*, p. arXiv:2305.04965
- González-Casanova D. F., Lazarian A., 2017, *ApJ*, **835**, 41
- Green D. A., 1993, *MNRAS*, **262**, 327
- Green C., Cunningham M., Dawson J., Jones P., Novak G., Fissel L., 2017, *The Astrophysical Journal Letters*, **887**
- HI4PI Collaboration et al., 2016, *A&A*, **594**, A116
- Ha T., Li Y., Kounkel M., Xu S., Li H., Zheng Y., 2022, *ApJ*, **934**, 7

- Hayes J. C., Norman M. L., Fiedler R. A., Bordner J. O., Li P. S., Clark S. E., ud-Doula A., Mac Low M.-M., 2006, *ApJS*, **165**, 188
- Heckman T. M., Baum S. A., van Breugel W. J. M., McCarthy P., 1989, *ApJ*, **338**, 48
- Heitsch F., Zweibel E. G., Mac Low M.-M., Li P., Norman M. L., 2001, *ApJ*, **561**, 800
- Ho K. W., Lazarian A., 2021, *ApJ*, **911**, 53
- Ho K. W., Lazarian A., 2023, *MNRAS*,
- Ho K. W., Yuen K. H., Lazarian A., 2021, *arXiv e-prints*, p. [arXiv:2111.06845](https://arxiv.org/abs/2111.06845)
- Ho K. W., Yuen K. H., Lazarian A., 2023, *MNRAS*,
- Hoang T. D., et al., 2022, *ApJ*, **929**, 27
- Hollenbach D. J., Tielens A. G. G. M., 1999, *Reviews of Modern Physics*, **71**, 173
- Hu Y., Lazarian A., 2022, *arXiv e-prints*, p. [arXiv:2210.11023](https://arxiv.org/abs/2210.11023)
- Hu Y., Lazarian A., 2023a, *arXiv e-prints*, p. [arXiv:2302.05047](https://arxiv.org/abs/2302.05047)
- Hu Y., Lazarian A., 2023b, *MNRAS*, **519**, 3736
- Hu Y., Yuen K. H., Lazarian A., 2018, *MNRAS*, **480**, 1333
- Hu Y., et al., 2019a, *Nature Astronomy*, **3**, 776
- Hu Y., Yuen K. H., Lazarian A., 2019b, *ApJ*, **886**, 17
- Hu Y., Yuen K. H., Lazarian A., 2020a, *ApJ*, **888**, 96
- Hu Y., Lazarian A., Yuen K. H., 2020b, *ApJ*, **897**, 123
- Hu Y., Lazarian A., Li Y., Zhuravleva I., Gendron-Marsolais M.-L., 2020c, *ApJ*, **901**, 162
- Hu Y., Lazarian A., Bialy S., 2020d, *ApJ*, **905**, 129
- Hu Y., Lazarian A., Stanimirović S., 2021, *ApJ*, **912**, 2
- Hu Y., Lazarian A., Wang Q. D., 2022a, *MNRAS*, **511**, 829
- Hu Y., Lazarian A., Wang Q. D., 2022b, *MNRAS*, **513**, 3493
- Hu Y., Lazarian A., Beck R., Xu S., 2022c, *ApJ*, **941**, 92
- Hwang J., et al., 2021, *ApJ*, **913**, 85
- Juvela M., 2016, *Astronomy & Astrophysics*, **593**, A58
- Kalberla P. M. W., Haud U., 2018, *A&A*, **619**, A58
- Kalberla P. M. W., Haud U., 2020, *arXiv e-prints*, p. [arXiv:2003.01454](https://arxiv.org/abs/2003.01454)
- Kalberla P. M. W., Haud U., 2023, *arXiv e-prints*, p. [arXiv:2303.16183](https://arxiv.org/abs/2303.16183)
- Kalberla P. M. W., Kerp J., 2016, *A&A*, **595**, A37
- Kalberla P. M. W., Kerp J., Haud U., 2021, *A&A*, **654**, A91
- Kalberla P. M. W., Kerp J., Haud U., 2022, *arXiv e-prints*, p. [arXiv:2202.01610](https://arxiv.org/abs/2202.01610)
- Kandel D., Lazarian A., Pogosyan D., 2016, *MNRAS*, **461**, 1227
- Khabarova O., 2017, in AGU Fall Meeting Abstracts. pp SH14A–01
- Kowal G., Lazarian A., Vishniac E. T., Otmianowska-Mazur K., 2009, *ApJ*, **700**, 63
- Koyama H., Inutsuka S.-i., 2002, *ApJ*, **564**, L97
- Krieger M. S., Sinai S., Nowak M. A., 2020, *Nature Communications*, **11**, 2192
- Kulkarni S. R., Heiles C., 1988, in Kellermann K. I., Verschuur G. L., eds., Galactic and Extragalactic Radio Astronomy. pp 95–153
- Lazarian A., 2009, *Space Sci. Rev.*, **143**, 357
- Lazarian A., Pogosyan D., 2000, *ApJ*, **537**, 720
- Lazarian A., Pogosyan D., 2004, *ApJ*, **616**, 943
- Lazarian A., Pogosyan D., 2012, *ApJ*, **747**, 5
- Lazarian A., Vishniac E. T., 1999, *ApJ*, **517**, 700
- Lazarian A., Yuen K. H., 2018a, *ApJ*, **853**, 96
- Lazarian A., Yuen K. H., 2018b, *ApJ*, **865**, 59
- Lazarian A., Pogosyan D., Esquivel A., 2002, in Taylor A. R., Landecker T. L., Willis A. G., eds, Astronomical Society of the Pacific Conference Series Vol. 276, Seeing Through the Dust: The Detection of HI and the Exploration of the ISM in Galaxies. p. 182 ([arXiv:astro-ph/0112368](https://arxiv.org/abs/astro-ph/0112368)), doi:[10.48550/arXiv.astro-ph/0112368](https://doi.org/10.48550/arXiv.astro-ph/0112368)
- Lazarian A., Yuen K. H., Lee H., Cho J., 2017, *ApJ*, **842**, 30
- Lazarian A., Yuen K. H., Ho K. W., Chen J., Lazarian V., Lu Z., Yang B., Hu Y., 2018, *ApJ*, **865**, 46
- Lazarian A., Yuen K. H., Pogosyan D., 2020, *arXiv e-prints*, p. [arXiv:2002.07996](https://arxiv.org/abs/2002.07996)
- Lazarian A., Yuen K. H., Pogosyan D., 2022, *ApJ*, **935**, 77
- Li P. S., Lopez-Rodriguez E., Ajeddig H., André P., McKee C. F., Rho J., Klein R. I., 2021, *MNRAS*,
- Liu M., Hu Y., Lazarian A., 2022, *MNRAS*, **510**, 4952
- Lu Z., Lazarian A., Pogosyan D., 2020, *MNRAS*, **496**, 2868
- Ma Y. K., et al., 2023, *arXiv e-prints*, p. [arXiv:2302.04880](https://arxiv.org/abs/2302.04880)
- Mac Low M.-M., Klessen R. S., 2004, *Reviews of Modern Physics*, **76**, 125
- Mangeney A., Alexandrova O., Rakoto V., Pantellini F., Zaslavsky A., Perrone D., Maksimovic M., Issautier K., 2014, in EGU General Assembly Conference Abstracts. EGU General Assembly Conference Abstracts. p. 10801
- Maron J., Goldreich P., 2001, *ApJ*, **554**, 1175
- McComb W. D., 1990, The physics of fluid turbulence
- McKee C. F., Ostriker J. P., 1977, *ApJ*, **218**, 148
- McKee C. F., Ostriker E. C., 2007, *ARA&A*, **45**, 565
- Men'shchikov A., 2013, *Astronomy & Astrophysics*, **560**, A63
- Mihalas D., Binney J., 1981, Galactic astronomy. Structure and kinematics
- Moffatt H. K., 1978, Magnetic field generation in electrically conducting fluids
- Molinari S., et al., 2010, *A&A*, **518**, L100
- Monin A., Yaglom A., 2013, Statistical Fluid Mechanics, Volume II: Mechanics of Turbulence. Dover Books on Physics, Dover Publications, <https://books.google.com/books?id=6xPEAgAAQBAJ>
- Montgomery D., Turner L., 1981, *Physics of Fluids*, **24**, 825
- Murray C. E., Peek J. E. G., Kim C.-G., 2020, *ApJ*, **899**, 15
- Ostriker E. C., Stone J. M., Gammie C. F., 2001, *ApJ*, **546**, 980
- Padoan P., Juvela M., Kritsuk A., Norman M. L., 2006, *ApJ*, **653**, L125
- Padoan P., Juvela M., Kritsuk A., Norman M. L., 2009, *ApJ*, **707**, L153
- Panopoulou G. V., Clark S. E., Hacar A., Heitsch F., Kainulainen J., Ntormousi E., Seifried D., Smith R. J., 2022, *A&A*, **657**, L13
- Pattle K., et al., 2021, *ApJ*, **907**, 88
- Peek J. E. G., Clark S. E., 2019, *ApJ*, **886**, L13
- Peek J. E. G., et al., 2018, *ApJS*, **234**, 2
- Perrone D., Alexandrova O., Mangeney A., Maksimovic M., Rocoto V., Pantellini F., Zaslavsky A., Issautier K., 2015, in EGU General Assembly Conference Abstracts. EGU General Assembly Conference Abstracts. p. 12706
- Planck Collaboration et al., 2015, *A&A*, **576**, A104
- Planck Collaboration et al., 2016, *A&A*, **586**, A135
- Planck Collaboration et al., 2020, *A&A*, **641**, A3
- Saffman P. G., 1981, in Jimenez J., ed., The Role of Coherent Structures in Modelling Turbulence and Mixing. pp 1–9, doi:[10.1007/3-540-10289-2_19](https://doi.org/10.1007/3-540-10289-2_19)
- Schekochihin A. A., Cowley S. C., Taylor S. F., Maron J. L., McWilliams J. C., 2004, *ApJ*, **612**, 276
- Schmaltz T., Hu Y., Lazarian A., 2022, *arXiv e-prints*, p. [arXiv:2210.12518](https://arxiv.org/abs/2210.12518)
- Shebalin J. V., Matthaeus W. H., Montgomery D., 1983, *Journal of Plasma Physics*, **29**, 525
- Skalidis R., Sternberg J., Beattie J. R., Pavlidou V., Tassis K., 2021, *A&A*, **656**, A118
- Sondhiya D. K., Gwal A. K., Kasde S. K., 2016, in 41st COSPAR Scientific Assembly. pp D2.4–6–16
- Stanimirović S., Lazarian A., 2001, *ApJ*, **551**, L53
- Stanimirović S., Staveley-Smith L., Dickey J. M., Sault R. J., Snowden S. L., 1999, *MNRAS*, **302**, 417
- Swift J. J., Welch W. J., 2008, *ApJS*, **174**, 202
- Teyssier R., 2002, *A&A*, **385**, 337
- Tram L. N., et al., 2022, *arXiv e-prints*, p. [arXiv:2205.12084](https://arxiv.org/abs/2205.12084)
- Tritsis A., Federrath C., Schneider N., Tassis K., 2018, *MNRAS*, **481**, 5275
- Tsinobis A., Levich E., 1983, *Physics Letters A*, **99**, 321
- Vlahos L., Islikier H., 2023, *arXiv e-prints*, p. [arXiv:2303.15351](https://arxiv.org/abs/2303.15351)
- Vogelsberger M., White S. D. M., Mohayaee R., Springel V., 2009, *MNRAS*, **400**, 2174
- Wakker B. P., van Woerden H., 1997, *ARA&A*, **35**, 217
- Xu S., Lazarian A., 2016, *ApJ*, **833**, 215
- Xu S., Zhang B., 2017, *ApJ*, **835**, 2
- Xu S., Ji S., Lazarian A., 2019, *ApJ*, **878**, 157
- Xu D., Law C.-Y., Tan J. C., 2023, *ApJ*, **942**, 95
- Yuen K. H., Lazarian A., 2017, *ApJ*, **837**, L24
- Yuen K. H., Lazarian A., 2020a, *ApJ*, **898**, 65
- Yuen K. H., Lazarian A., 2020b, *ApJ*, **898**, 66
- Yuen K. H., Hu Y., Lazarian A., Pogosyan D., 2019, *arXiv e-prints*, p. [arXiv:1904.03173](https://arxiv.org/abs/1904.03173)

Yuen K. H., Ho K. W., Lazarian A., 2021, *ApJ*, **910**, 161

Yuen K. H., Ho K. W., Lazarian A., 2022a, *arXiv e-prints*, p. [arXiv:2202.07871](https://arxiv.org/abs/2202.07871)

Yuen K. H., Ho K. W., Law C. Y., Chen A., Lazarian A., 2022b, *arXiv e-prints*, p. [arXiv:2204.13760](https://arxiv.org/abs/2204.13760)

Yuen K. H., Chen A., Ho K. W., Lazarian A., 2023a, *MNRAS*, **519**, 2701

Yuen K. H., Yan H., Lazarian A., 2023b, *MNRAS*, **521**, 530

APPENDIX A: WHAT DOES THE CORRELATION BETWEEN THIN CHANNEL MAPS AND FIR MAP TELL US?

The ΔI_{857} parameter is introduced by [Clark et al. \(2019\)](#) to quantify the correlation between HI thin channel maps and Planck 857 GHz FIR map. ΔI_{857} for a given channel with width Δv can be written as:

$$\begin{aligned} \Delta I_{857} &= \frac{\langle I_{857} \omega \rangle - \langle I_{857} \rangle \langle \omega \rangle}{\langle \omega \rangle} \\ &= \langle I_{857} \rangle \left(\frac{\langle I_{857} \omega \rangle}{\langle I_{857} \rangle \langle \omega \rangle} - 1 \right), \end{aligned} \quad (\text{A1})$$

where I_{857} is the intensity of Planck 857 GHz dust emission, which is dominated by thermal dust and is proportional to dust column density. ω is the USM-measured intensity fluctuations of the HI channel. ΔI_{857} essentially measures the cross-correlation between I_{857} and channel fluctuations. ΔI_{857} is normalized by the mean USM intensity $\langle \omega \rangle$. However, another normalization by the mean I_{857} is missing, which adds difficulty in making conclusions based on the parameter magnitude.

Below we analytically make the physical meaning of ΔI_{857} clear. Consider two signals, one, I_{857} , proportional to the local column density, and another, ω , proportional to the PPV intensity ρ_s . The two can be expressed as:

$$\begin{aligned} I_{857}(\mathbf{X}_1) &\propto \int \rho_s(\mathbf{X}_1, v) dv \equiv \rho_c(\mathbf{X}_1), \\ \omega(\mathbf{X}_2) &\propto \int^{\Delta v} \rho_s(\mathbf{X}_2, v) dv \equiv \rho_s^{\Delta v}(\mathbf{X}_2, v), \end{aligned} \quad (\text{A2})$$

where $\mathbf{X} = (x, y)$ represents the position vector on the POS. ρ_c is column density and $\rho_s^{\Delta v}(\mathbf{X}, v)$ is a PPV channel with width Δv . Note there $\rho_s(\mathbf{X}, v) = \int \rho(\mathbf{X}, z) \phi(v - v_{\text{tur}}(\mathbf{X}, z)) dz$ is mapped from density $\rho(\mathbf{X}, z)$ in PPP space, where ϕ is a Maxwellian distribution of the residual thermal velocity by subtracting turbulent velocity $v_{\text{tur}}(\mathbf{X}, z)$ from LOS velocity v .

It is clear now that if the turbulent velocities $v_{\text{tur}}(\mathbf{X}, z)$ are uncorrelated¹¹ with the density $\rho(\mathbf{X}, z)$, velocity factor gives rise to the same multiplier $\phi_v^{\Delta v} \equiv \int^{\Delta v} dv \langle \phi(v - v_{\text{tur}}(\mathbf{X}, z)) \rangle$ in all the averages of Equation (A1). Then we have:

$$\begin{aligned} \langle \omega \rangle &\propto \langle \rho_s^{\Delta v}(v) \rangle \approx \phi_v^{\Delta v} \langle \rho_c \rangle, \\ \langle I_{857} \omega \rangle &\propto \langle \rho_c(\mathbf{X}_1) \rho_s^{\Delta v}(\mathbf{X}_2, v) \rangle \approx \phi_v^{\Delta v} \langle \rho_c(\mathbf{X}_1) \rho_c(\mathbf{X}_2) \rangle. \end{aligned} \quad (\text{A3})$$

As a result, the correlation can be written as:

$$\frac{\langle I_{857} \omega \rangle}{\langle I_{857} \rangle \langle \omega \rangle} \approx \frac{\langle \rho_c(\mathbf{X}_1) \rho_c(\mathbf{X}_2) \rangle}{\langle \rho_c \rangle^2}, \quad (\text{A4})$$

and accordingly ΔI_{857} is:

$$\Delta I_{857} = \langle I_{857} \rangle \left(\frac{\langle \rho_c(\mathbf{X}_1) \rho_c(\mathbf{X}_2) \rangle}{\langle \rho_c \rangle \langle \rho_c \rangle} - 1 \right). \quad (\text{A5})$$

Apparently, ΔI_{857} is insensitive to the uncorrelated velocity contribution but measures the level of fluctuations in column density. The value of ΔI_{857} is not normalized, rather is bounded by $\langle I_{857} \rangle$. Although our considerations were idealized, they do illustrate that the correlation measure in Eq. A1 is not suitable to draw conclusions about the level of velocity caustics in channel maps.

APPENDIX B: ISOTHERMAL MHD TURBULENCE SIMULATIONS

We present a supersonic MHD simulation ($M_S = 10$ and $M_A = 0.7$) in Fig. B1, comparing thick and thin (central and wing) channels with thermal broadening included. However, we do not observe any significant resemblance between the thick and thin (central and wing) channels, which differs from the findings of [Clark et al. \(2019\)](#) using 128^3 hydrodynamic simulations. This is expected since, in supersonic conditions (usually in molecular clouds), the thermal speed is considerably smaller than the turbulent velocity, resulting in a minimal contribution of thermal broadening.

The thermal broadening effect is more important for the low- M_S case. Thus, we conducted a test to assess the impact of thermal broadening on velocity caustics. To do this, we artificially increased the thermal speed in the isothermal $M_S = 1.2$, $M_A = 0.6$ MHD simulations and compared the wing thin channels p and the pure velocity caustic channel p_{vc} , obtained by applying simulation velocities to constant density (as in Fig. 2). In other words, p_{vc} removes any pre-existing density structures. In Fig. B2, we observe that in the normal $\sigma_T = c_s$ case, the intensity structures in p are similar to those in p_{vc} , but differences are also present. When σ_T increases (i.e., stronger thermal broadening), the intensity structures in p change further. This is expected (see § 3), see thermal broadening can decrease the velocity contribution in a channel. However, the results in Fig. B2 suggest that the thermal broadening at a normal level ($\sigma_T = c_s$) is marginal in erasing velocity contribution¹².

Nevertheless, VDA was proposed as an effective approach to removing contamination from thermal broadening ([Yuen et al. 2021](#)). In Fig. B2, we test VDA's performance by artificially varying the significance of thermal broadening from $\sigma_T = c_s$ to $\sigma_T = 2c_s$. We can see that the VDA-decomposed velocity contribution p_v maps are highly similar in all cases. The p_v maps resemble the p_{vc} map well, even though the thermal broadening effect is stronger than the normal level.

APPENDIX C: RHT PROCESSED THIN CHANNEL MAPS

In order to carry out the RHT analysis, three input parameters are needed: smoothing kernel diameters (DK), a window diameter (DW), and an intensity threshold (Z). Fig. C1 displays the RHT-processed thin channel map $p(x, y, z)$, which is used in Fig. 7, with varying input parameters. Notably, we observed significant differences in the results for the different cases. The parameter DW controls the straightness of the RHT-fibers, while DK determines the thickness. Z

¹¹ This property is numerically and observationally demonstrated (see Fig. 6 and [Yuen et al. 2021](#); [Kalberla et al. 2022](#); [Yuen et al. 2022a](#)).

¹² Note that p_{vc} is generated from a constant density cube with $\sigma_T = c_s$. If thermal broadening erases all velocity information, p_{vc} should be only a uniform-intensity map.

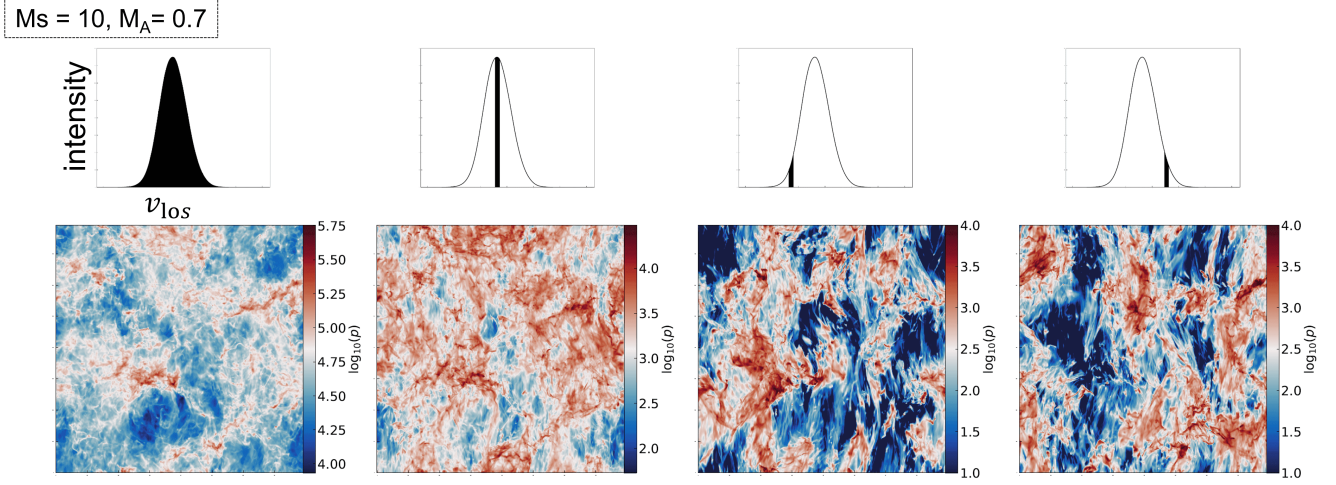


Figure B1. Comparisons of thick velocity channel (left) and thin center and wing channels. The synthetic line is generated by using a non-constant 3D density field ρ from the supersonic MHD simulation. The velocity range used for integration is indicated by the shaded region in the top spectrum. The mean magnetic field is oriented along the vertical y -direction and thermal broadening is included.

$M_S = 1.2$
 $M_A = 0.6$

(a) MHD simulation: non-constant $\rho(x, y, z)$

(b) Constant $\rho(x, y, z)$

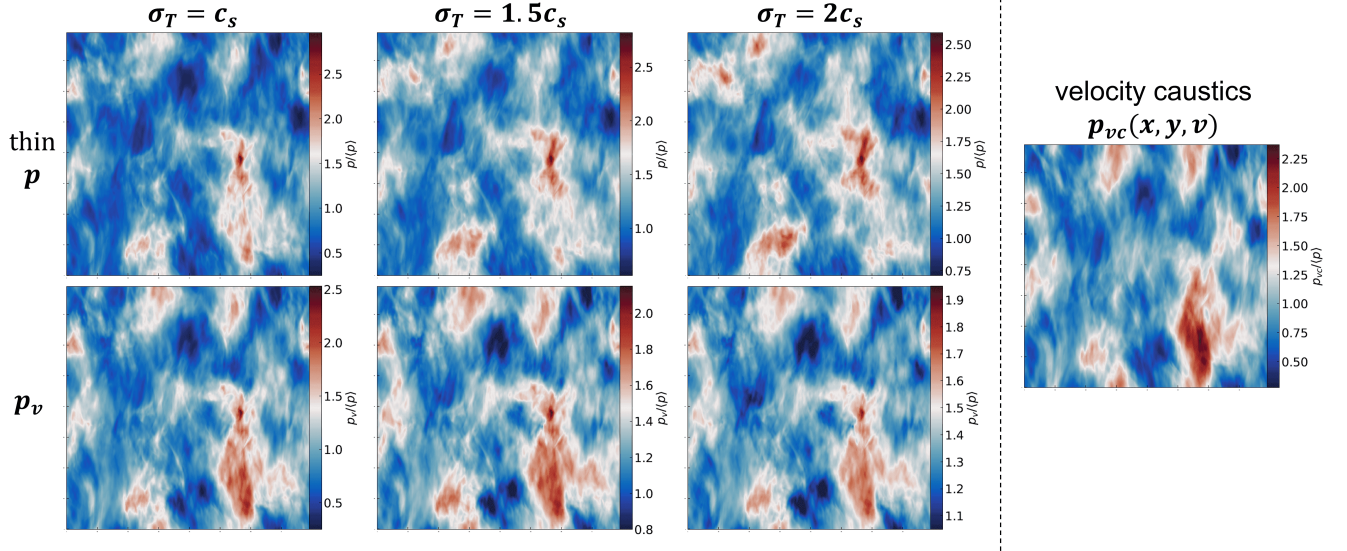


Figure B2. Panel (a): Comparisons of thin channels p (top) and VDA-decomposed velocity contribution p_v with different thermal kernels σ_T . Larger σ_T means stronger thermal broadening. The synthetic line is generated by using a non-constant 3D density field ρ from the $M_S = 1.2, M_A = 0.6$ MHD simulation. The channel width is identical to the thin channel used in B1. The mean magnetic field is oriented along the vertical y -direction. **Panel (b):** The thin channel in this panel was generated using a constant density field, thereby eliminating any pre-existing density structures. The structures within the thin channel are solely created by velocity caustics, and thus we refer to it as the velocity caustics channel p_{vc} . The integration velocity range is identical to that in panel (a).

regulates the intensity threshold for blanking out low-intensity structures. The RHT-fibers' orientation varies significantly with different input parameters (see Figs. 5, 6, 7 in Clark et al. 2014). Especially, the parameter DK would significantly change the aspect ratios of identified RHT-fibers.

Using the parameters DK = 11, DW = 55, Z = 0.7, we generated RHT-maps for the HI cloud shown in Fig. 7 with different chan-

nel widths ($\Delta v \approx 0.2, 4.0, 27, 55$ km/s). Fig. C2 displays the channel maps and RHT-maps. The channel maps exhibit similar filamentary structures when $\Delta v \approx 0.2, 4.0$ km/s, while the striations become less noticeable for thicker channels. The RHT-maps ($\Delta v \approx 0.2$ and 4.0 km/s) are comparable, with RHT-fibers aligning with the magnetic field (as shown in Fig. 7). The same trend is observed in the other

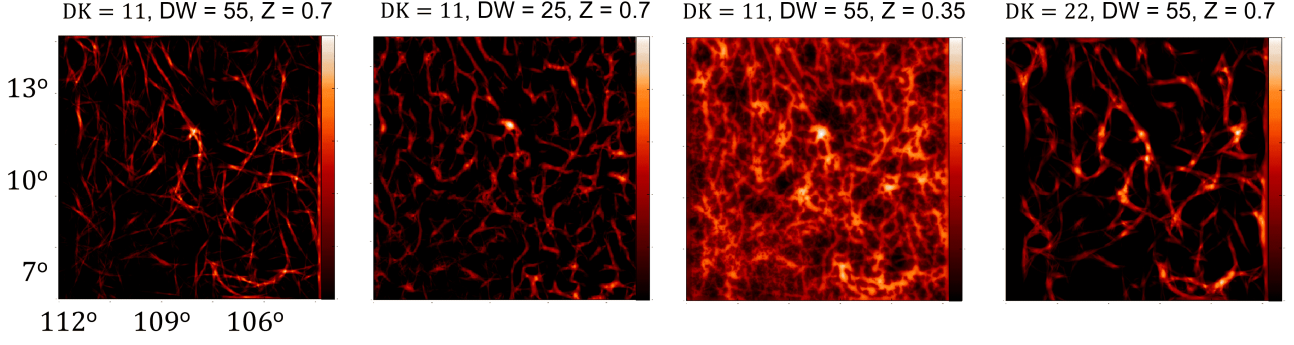


Figure C1. RHT-processed HI thin channel maps (see Fig. 7) with different input parameters.

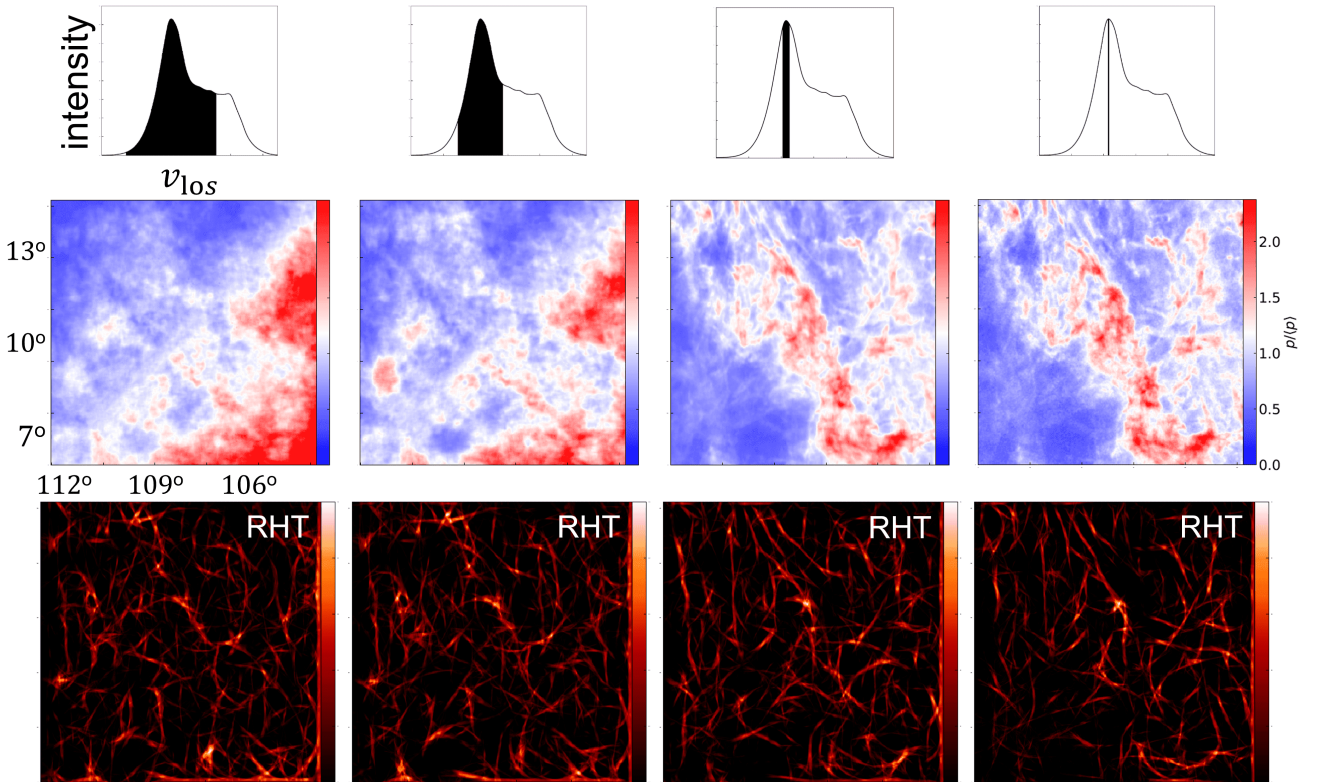


Figure C2. Comparison of HI thin channel maps (middle), as well as their corresponding RHT-maps (bottom) with different channels width ($\Delta v \approx 0.2, 4.0, 27, 55$ km/s from right to left). The velocity range used for integration is indicated by the shaded region in the spectrum (top).

two RHT-maps ($\Delta v \approx 27$ and 55 km/s), but perpendicular RHT-fibers become more prominent (see Fig. 7).

It should be noted that the changes in channel maps and RHT-maps could be due to the projection of multiple HI clouds. Specifically, if the cold-filament hypothesis is correct, the perpendicular RHT-fibers should have higher intensities and be visible in other thin channels ($\Delta v \approx 0.2$). To investigate this possibility, Fig. C3 presents four thin channels and their RHT-maps ($DK = 11$, $DW = 55$, $Z = 0.7$) located at different $v_{\text{los}} \approx 3, -14, 23, 43$ km/s. Their LOS velocity difference (~ 20 km/s) is greater than the typical turbulent velocity dispersion. In all four channels, the HI striations exhibit

morphological differences, but all tend to align with the magnetic field (as shown in Fig. E1 for the magnetic field map). The wing channels' intensities ($v_{\text{los}} \approx -14, 23, 43$ km/s) are smaller than those in the central channel ($v_{\text{los}} \approx 3$ km/s). In terms of the RHT-maps, no apparent perpendicular RHT-fibers are visible, while such fibers are observed in the upper part of thick channels and the FIR map (as illustrated in Figs. 7 and C2). This simple test excludes the possibility of the LOS projection effect.

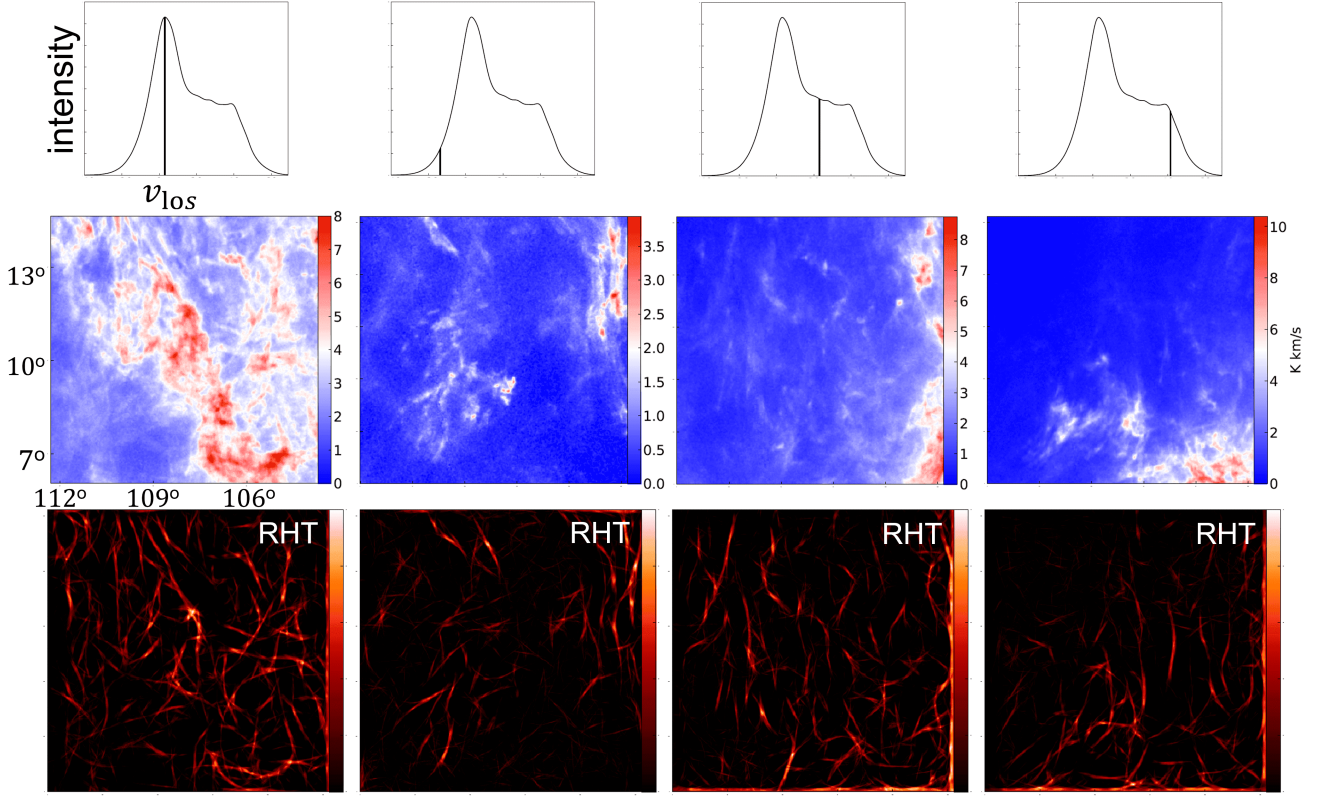


Figure C3. Same as Fig. C2, but for HI thin channel map $\Delta v \approx 0.2$ km/s at different $v_{\text{los}} \approx 3, -14, 22, 42$ km/s (from right to left).

APPENDIX D: VDA DECOMPOSED GALFA-HI THIN CHANNEL

Fig. D1 displays a visual comparison between the VDA-separated velocity contribution p_v , density contribution p_d , and the raw thin channel p for two more HI clouds (one high-latitude and one low-latitude) with central coordinates (R.A., Dec.) = (212.00°, 10.35°) and (268.00°, 26.35°). The channel width is $\Delta v \approx 0.2$ km/s. For the (212.00°, 10.35°) cloud, p and p_v are highly similar with NCC values of ≈ 0.63 for $v_{\text{los}} \approx -2.3$ km/s and ≈ 0.71 for $v_{\text{los}} \approx -10$ km/s suggesting the dominance of velocity contribution in thin channels. The situation is more complicated for the (268.00°, 26.35°) cloud, the similarity of p_v and p is observed only in the bottom half map for $v_{\text{los}} \approx 4.0$. This indicates possible equipartition of velocity and density contributions in this particular velocity channel (Yuen et al. 2021). We obtain NCC ≈ 0.50 for this channel, while ≈ 0.53 for the one with $v_{\text{los}} \approx 10.0$ km/s.

APPENDIX E: COMPARISONS OF VCHGS AND RHT

Fig. E1 presents a comparison of magnetic field morphology derived from VChGs, Planck 353 GHz polarization, and RHT. For VChGs calculation, we adopt the recipe used in Hu & Lazarian (2023a). We calculate the gradient in every $\Delta v \approx 0.2$ km/s channel (gradients are blanked out if their associated HI intensity is less than three times the noise level) and average the gradient over 16×16 cells sub-block to get the VChGs orientation. In order fairly compare with Planck polarization, VChGs is then used to construct pseudo-Stokes parameters Q_g and U_g and integrated over the full velocity range

from -40 km/s to 70 km/s. The final POS magnetic field orientation is derived from $\phi_B = \frac{1}{2} \arctan(U_g, Q_g) + \frac{\pi}{2}$.

For RHT, we follow Clark & Hensley (2019) for calculation. We applied a kernel bar (DW) of the length of 25 pixels and the histogram fraction threshold (Z) was taken at 0.7 of the maximum. The smoothing window (DK) was set to 5 pixels. The procedure was repeated for every velocity channel at the native GALFA spectral resolution ($\Delta v \approx 0.2$ km/s). The RHT angle then is averaged over the velocity range of $[-40, 70]$ km/s and projected into the POS. Finally, we smooth the POS magnetic field orientation inferred from RHT to match the resolution of VChGs.

As shown in Fig. E1, the magnetic field for this cloud (see Fig. 7) orients almost along the north-south direction. An apparent variation of magnetic field appears at the lower left corner in Planck and VChGs' maps, while such variation is not observed in the RHT map. In Fig. E2, we plot the histogram of the magnetic field angle in IAU convention inferred from the three methods. We can see VChGs shows better agreement with Planck than RHT. The VChGs and Planck angles are widely spreading from -90 to 90 degrees, while the RHT angle is less dispersed concentrating in the range of $[-25, 25]$ degrees.

We define the **Alignment Measure** (AM) to quantify the alignment of the magnetic field derived from VChGs (also RHT) and the Planck polarization: $AM = 2\langle \cos^2 \theta_r - \frac{1}{2} \rangle$, where θ_r is the relative angle between the POS magnetic field inferred from two methods. A value of $AM = 1$ indicates a perfect parallel alignment, while $AM = -1$ represents a perpendicular alignment. The AM of VChGs and Planck achieves ~ 0.81 , while it is ~ 0.66 for RHT and Planck. While it is possible to achieve higher AM values by adjusting the

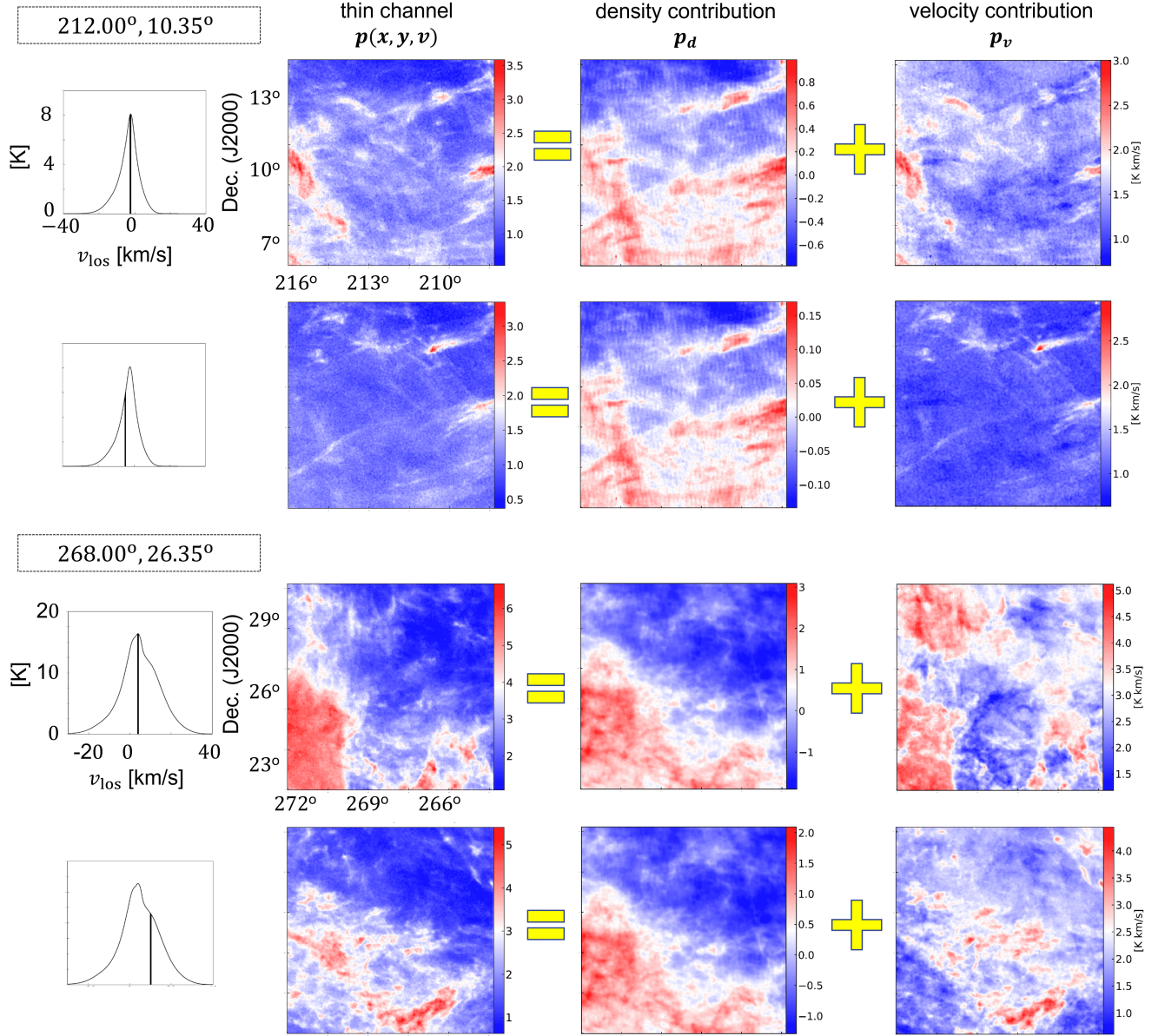


Figure D1. Same as Fig. 5, but for other two HI clouds with central coordinates are (R.A., Dec.) = (212.00°, 10.35°) and (268.00°, 26.35°), as well as central $v_{\text{los}} \approx -2.3$ and -10 km/s for the former and $v_{\text{los}} \approx 4.0$ and 10 km/s for the later. The channel width is $\Delta v \approx 0.2$ km/s.

input parameters, the physical meanings of the parameters are not clear. Nevertheless, the higher AM value suggests the parameter-free VChGs is more accurate in tracing magnetic fields.

On the other hand, VChGs is also able to derive the POS Alfvén Mach number M_A distribution. The physical reason behind it is that a strong magnetic field (i.e., small M_A) induces strong anisotropy, which corresponds to a narrow histogram (i.e., small dispersion) of the velocity gradient orientation. For a weak magnetic field (i.e., large M_A), the histogram tends to be isotropic with a large dispersion. This relation of M_A and velocity gradient orientation's dispersion was proposed in Lazarian et al. (2018) and successfully used to derive the M_A distribution in 3D over our Galaxy (Hu & Lazarian 2023a) with the assistance of the Galactic rotational curve. Here we follow the same recipe used in Hu & Lazarian (2023a) (see their Sec. 3)

to find the M_A distribution for the GALFA-HI cloud presented in Fig. E1. As shown in Fig. E3, the M_A is calculated for every 16×16 pixels. We find this HI cloud is globally sub-Alfvénic with a mean M_A of ~ 0.63 .

This paper has been typeset from a \LaTeX file prepared by the author.

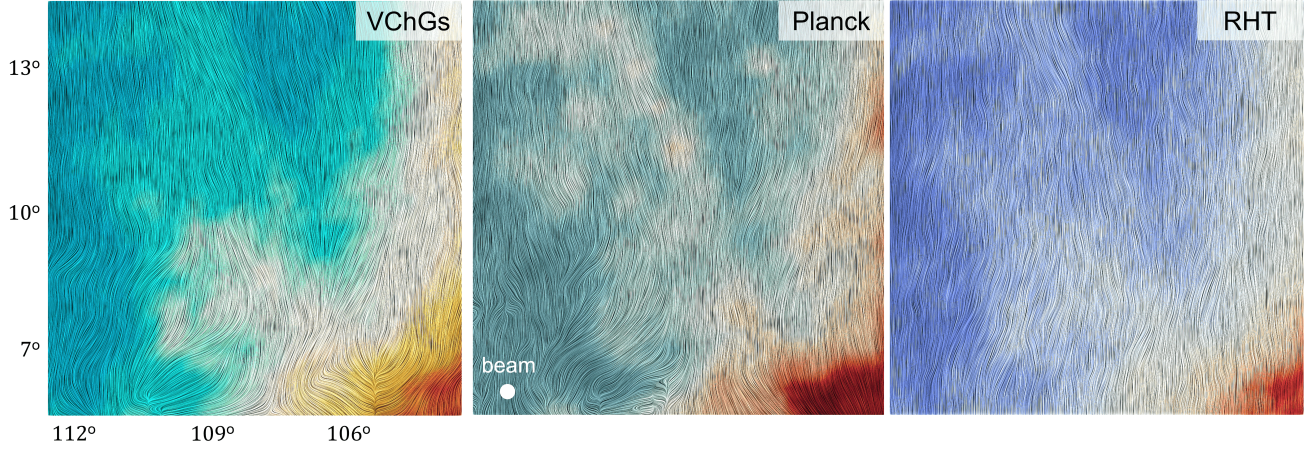


Figure E1. Magnetic field morphology derived from VChGs (left, background image: integrated HI intensity map), Planck 353 GHz polarization (the 2nd panel, background image: Planck FIR map), and RHT (the 3rd panel, background image: integrated HI intensity map) for the GALFA-HI cloud presented in Fig. 7.

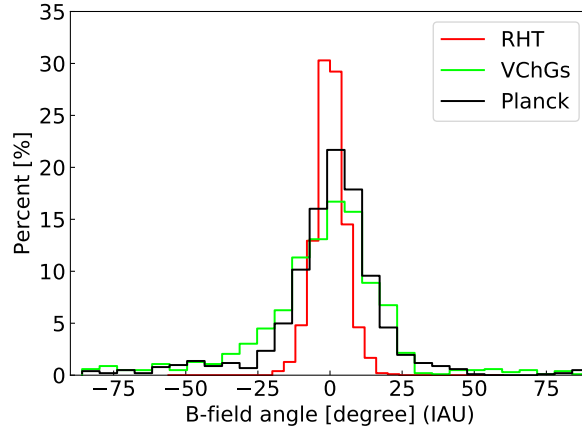


Figure E2. Histogram of magnetic field angle in IAU convention inferred from VChGs, Planck 353 GHz polarization, and RHT for the GALFA-HI cloud presented in Fig. E1.

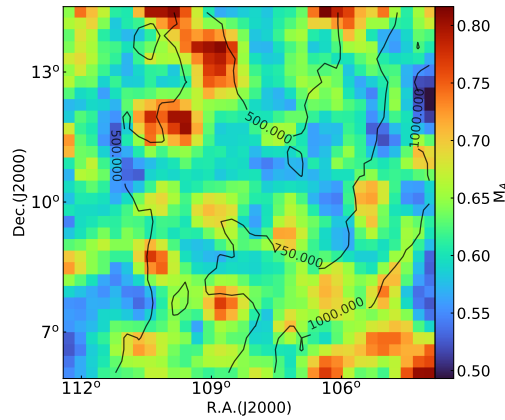


Figure E3. Map of the Alfvén Mach number M_A distribution derived from VChGs. The contours (in unit of K km/s) highlight prominent structures in the GALFA-HI cloud presented in Fig. E1.